

AD-A128 981

X-RAY COMPUTED TOMOGRAPHY FOR AEROSPACE COMPONENTS(U)
SCIENTIFIC MEASUREMENT SYSTEMS INC AUSTIN TX
F HOPKINS ET AL. JAN 83 AFWAL-TR-82-4128

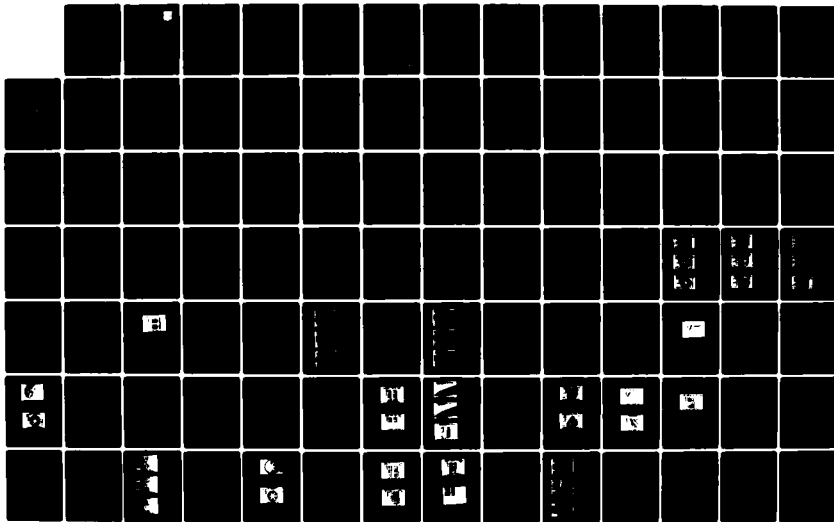
1/2

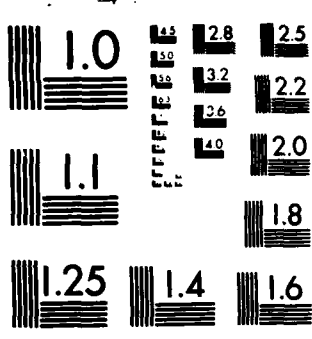
UNCLASSIFIED

F33615-80-C-5145

F/G 20/6

NL





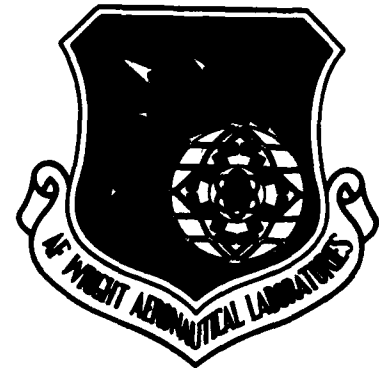
MICROCOPY RESOLUTION TEST CHART
NATIONAL BUREAU OF STANDARDS-1963-A

AFWAL-TR-82-4128

12

X-RAY COMPUTED TOMOGRAPHY FOR AEROSPACE COMPONENTS

AD 128981



Scientific Measurement Systems, Inc.
2808 Longhorn Boulevard, Suite 303
Austin, Texas 78759

January 1983

FINAL REPORT FOR September 1980 - January 1983

APPROVED FOR PUBLIC RELEASE: DISTRIBUTION UNLIMITED

MATERIALS LABORATORY
AIR FORCE WRIGHT AERONAUTICAL LABORATORIES
AIR FORCE SYSTEMS COMMAND
WRIGHT-PATTERSON AIR FORCE BASE, OHIO 45433

DTIC FILE COPY

DTIC
ELECTRONIC
S JUN 6 1983
A

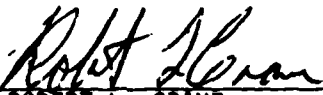
83 06 06 008

NOTICE

When Government drawings, specifications, or other data are used for any purpose other than in connection with a definitely related Government procurement operation, the United States Government thereby incurs no responsibility nor any obligation whatsoever; and the fact that the government may have formulated, furnished, or in any way supplied the said drawings, specifications, or other data, is not to be regarded by implication or otherwise as in any manner licensing the holder or any other person or corporation, or conveying any rights or permission to manufacture use, or sell any patented invention that may in any way be related thereto.

This report has been reviewed by the Office of Public Affairs (ASD/PA) and is releasable to the National Technical Information Service (NTIS). At NTIS, it will be available to the general public, including foreign nations.

This technical report has been reviewed and is approved for publication.



ROBERT L. CRANE

Nondestructive Evaluation Branch
Metals and Ceramics Division

FOR THE COMMANDER



DONALD M. FORNEY, JR., Chief
Nondestructive Evaluation Branch
Metals and Ceramics Division

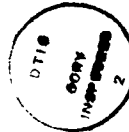
*If your address has changed, if you wish to be removed from our mailing list, or if the addressee is no longer employed by your organization please notify AFWAL/MLLP, W-PAFB, OH 45433 to help us maintain a current mailing list".

Copies of this report should not be returned unless return is required by security considerations, contractual obligations, or notice on a specific document.

PREFACE

This document constitutes the preliminary final report on Contract Number F33615-80-C-5145, between Scientific Measurement Systems, Inc., and Wright Patterson Air Force Base. It contains a study of the optimization of certain parameters of computed tomography systems for inspection of aerospace components, in general, and solid propellant rocket motors, in particular. The report consists of a series of computer simulations and empirical measurements which treat specific cases of appropriate phantoms. The phenomena of beam hardening and scattering, which can occur extensively in high energy, industrial tomography, are investigated in detail.

The report is organized into an introduction section, a theory and background section, a simulation section, a measurements section, and a conclusions and recommendations section. The primary finding is that computed tomography appears to be a feasible, new method for non-destructive inspection of solid propellant rocket motors, as well as other aerospace components.



PREVIOUS PAGE IS BLANK

SEARCHED	INDEXED
SERIALIZED	FILED
APR 1981	
FBI - MEMPHIS	
A	

PREVIOUS PAGE BLANK - NOT FILLED

Table of Contents

	Page
I. INTRODUCTION	1
II. THEORETICAL AND EMPIRICAL CONSIDERATIONS	7
1. SPECTRAL CONSIDERATIONS	7
a. Photon-matter interactions	7
b. Extraction of densities from attenuation	11
c. Beam hardening	15
2. SCATTERING EFFECTS	22
a. Scattering processes	22
b. Scattering simulations: Monte Carlo	28
3. SCATTERING SIMULATIONS	33
a. Object scattering	33
b. Interdetector scattering	37
III. SIMULATIONS OF A PHANTOM ROCKET MOTOR	40
1. MID-SECTION REGION	40
2. NOSE REGION	54
IV. EMPIRICAL SCANNING OF ROCKET MOTOR PHANTOMS	58
1. LARGE ROCKET MOTOR PHANTOM	58
a. Description of phantom	58
b. Apparatus and parametric specification	61
c. Tomograms and analysis	65

PREVIOUS PAGE
IS BLANK

Table of Contents (Concluded)

	Page
2. SMALL ROCKET MOTOR PHANTOM	77
a. Fabrication and scanning	77
b. Tomograms and analysis	79
V. CONCLUSIONS AND RECOMMENDATIONS	85
REFERENCES	88

List of Illustrations

	Page
Figure 1. Fan Beam Geometry	4
Figure 2. Photon Attenuation Coefficients	8
Figure 3. Bremsstrahlung Spectra	13
Figure 4. Graph Displaying the Compton Scattering	25
Figure 5. Graph of Maximum and Minimum Energy	26
Figure 6. Graph of Scattered to Direct Radiation	27
Figure 7. Cross Sectional Views of TOMOS Geometry	29
Figure 8. Simulated Tomograms of 457 mm Diameter Rocket Motor Phantom	43
Figure 9. Simulated Tomograms of Radial Cracks	44
Figure 10. Simulated Tomograms of Radial Cracks	45
Figure 11. Region of 1.27 mm Crack with Analysis Frames	48
Figure 12. Simulated Tomograms of Radial Cracks for Sources and Averaging	51
Figure 13. Simulated Tomograms of Radial Cracks with Scattering and Corrections	53
Figure 14. Drawing of Geometry of Simulated Nose Region	56
Figure 15. Simulated Tomograms of Delaminations in Nose Region	57
Figure 16. Drawing of Large Rocket Motor Phantom	59
Figure 17. Photogram and Tomogram of 470 mm Phantom	60
Figure 18. Block Diagram of SMS Industrial Tomographic Scanner System	62
Figure 19. Tomograms of Radial Cracks in 470 mm Phantom	66
Figure 20. Tomograms of Delaminations	67

List of Illustrations (Concluded)

	Page
Figure 21. Tomograms of Cylindrical Holes	69
Figure 22. Tomograms of Aluminum Rods	70
Figure 23. Analysis Frames for Radial Cracks	71
Figure 24. Vertical Density Traces	76
Figure 25. Photograph and Tomogram of 129 mm Diameter Phantom	78
Figure 26. Radial Cracks in 129 mm Phantom	80
Figure 27. Tomograms of Delamination in 129 mm Phantom	81
Figure 28. Vertical Density Traces in 129 mm Phantom	83

List of Tables

	Page
Table 1. Isotopic X-ray Sources	12
Table 2. Transmission and Beam Hardening of Bremstrahlung Spectra	18
Table 3. Empirical Fits to Mass-versus- Attenuation Function in Carbonaceous Material	20
Table 4. Coefficients of Fits to Mass Functions for Bremstrahlung Spectra and Isotopic Sources	21
Table 5. Interdetector Scattering Coefficients	32
Table 6. Monte Carlo Object Scattering Coefficients	35
Table 7. Calculated Interdetector Scattering Coefficients	39
Table 8. Average Densities Within Simulated Tomograms of 457 mm Phantom	47
Table 9. Frame Analysis Values for Radial Cracks in Computer	50
Table 10. Frame Analysis Values for Radial Cracks in 470 mm Phantom	73
Table 11. Frame Analysis for Aluminum Rods and Holes in 470 mm Phantom	74
Table 12. Frame Analysis Values for Radial Cracks in 129 mm Phantom	82

I. INTRODUCTION

The application of computerized tomography (CT), or computerized axial tomography (CAT), to the nondestructive evaluation of aerospace components requires consideration of various aspects of the technique as it is now utilized in medical diagnostics. The most significant difference to be encountered in the CT scanning of inanimate objects considerably denser than the human anatomy is the required use of higher source photon energies. Such photons provide penetration sufficient to yield reasonable transmission rates and signal-to-noise ratios (SNR).

Several consequences arise as a result of the use of high energy photons to measure attenuation and opacity along several different paths through an object. High energy here is taken to mean from a few hundred kiloelectron volts (keV) to several million electron volts (MeV). Two of the foremost are the effects of beam hardening, where polychromatic sources are employed, and the multiple scattering of photons, which leads eventually to the erroneous recording of signal strength in the detector assembly. The former can be minimized by choice of source energy, causing even less ambiguity than in medical situations. The latter requires an assessment of optimized shielding configuration in a scanner and software correction procedures to remove residual effects.

The degree to which beam hardening or scattering affects tomographic data depends largely upon the masses encountered in the object of interest. The general category of aerospace components encompasses an extremely wide range of shapes, sizes, and total densities, from low density carbon composite structures, limited sizes of which can be scanned effectively with conventional medical tomographs, to complicated aircraft and missile assemblies of several feet in dimensions. The intent in the present

investigation was to concentrate on solid propellant rocket motors and the critical inspection problems that are well known for those objects. Further, the majority of attention in both simulations and empirical scanning was given to one specific geometry, a motor of approximate outside diameter of 45 cm. Conclusions are drawn for other geometries based on those results, as well as more generalized treatments of the phenomena.

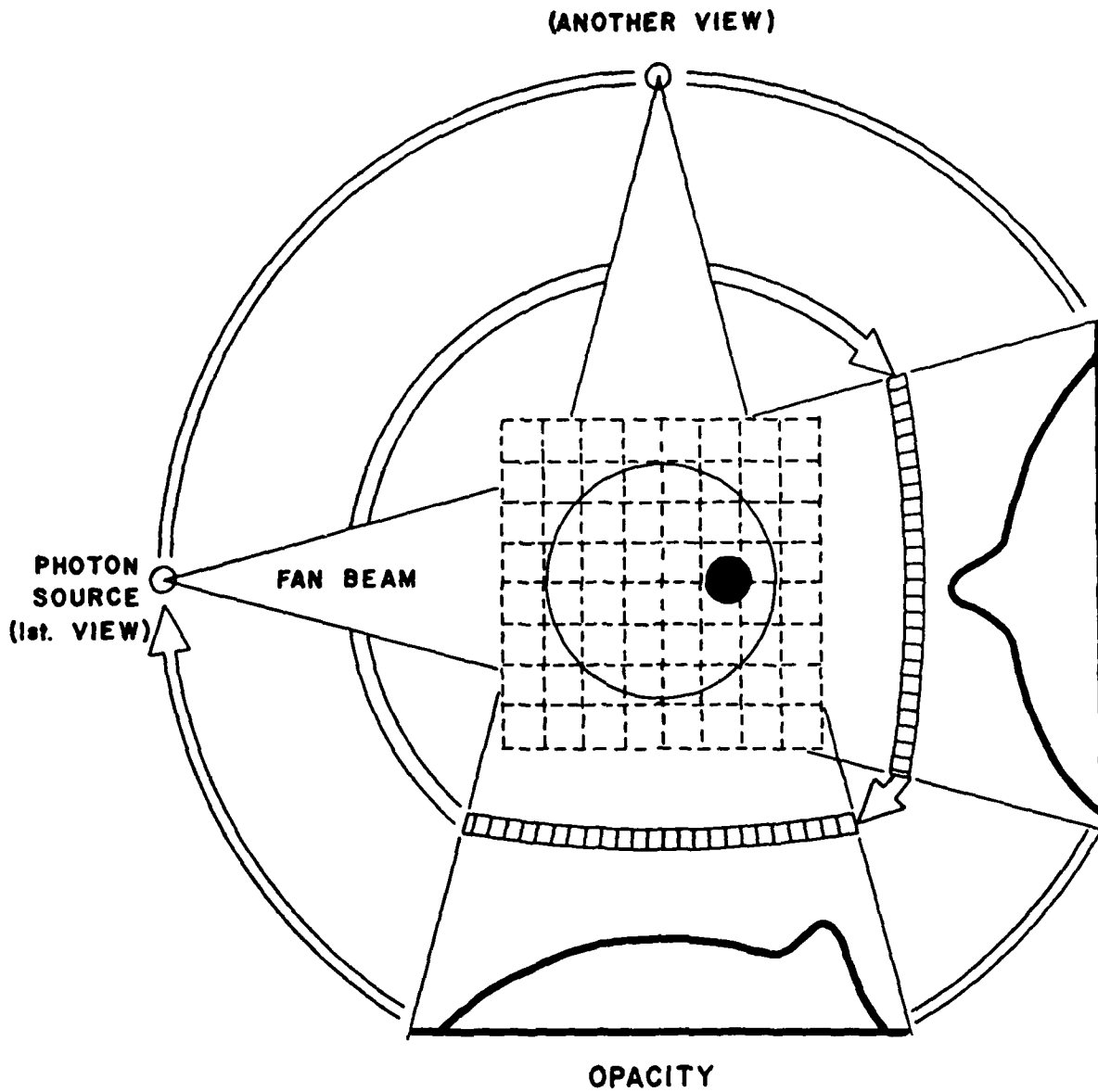
The emphasis in these studies was upon the characterization of the effects of the processes, and determination of appropriate preventative or corrective procedures for optimization of probability of detection of a selected group of features. Most importantly, these included cracks in the solid propellant and debonding or delamination between propellant and adjacent interface materials such as cork. In addition, for a few selected cases, examples of the effects of spatial resolution and statistical accuracy of projection data were obtained, in order to provide a qualitative test of the interplay between the effects of the photon-matter interaction phenomena and basic tomographic parameters. A simplified pattern recognition analysis has been applied to several of the tomograms, which allows some quantification beyond the usual visual interpretation of the density values represented in a tomogram. A comprehensive version of such an approach is a likely candidate for the eventual mode of inspection of certain aerospace components with photon tomography.

In addition to the diversity of characteristics of aerospace objects which potentially could be inspected by CT, there are several possible configurations of scanner systems which merit attention. Three basic geometries have been used in recent years in medical tomography. They are generally referred to as second generation (SG), third generation (TG), and fourth generation (FG).

The SG design consists of a fan beam of source photons impinging upon an array of detector elements, the width of which defines the total angle of the fan. Sampling of opacity values through the object is accomplished by translating the fan linearly across the object, indexing the angle of the axis of translation, translating again, and repeating this process. Spacing between adjacent rays is determined by the increment of translation. The form of the data generated is a set of parallel rays with variable ray spacing, depending upon position within the fan. In industrial scanning, the rotational and translational motions may be achieved by appropriate motion of the object, the scanner system itself, or a combination of both, depending upon such factors as the desired mechanical simplicity, speed of data acquisition, and cost of the system.

The TG geometry also employs a fan beam of flux. However, instead of coupling rotational and translational motions to provide ray paths of sampling, rotation alone with a fine angular increment suffices. Figure 1 represents such a geometry. Generally, the intrinsic spacing between adjacent detectors in the tightly packed array serves directly as the ray spacing. In medical TG systems, the detectors are of a few mm width and nearly contiguous. In industrial situations, where slower scanning speeds and hence fewer detectors may be tolerated and/or interdetector shielding may be needed, the detectors may be spaced somewhat. In the latter case, the desired ray spacing and ray density within the fan may be obtained by indexing the detector assembly on a radius from the source over one detector spacing. The projection data is fan-beam in nature.

The most recently developed configuration is known as fourth generation. It consists of a fixed ring of detectors, regularly spaced about 360 deg. The source rotates about the object, generating a fan of data for each detector. In this case, the detector is at the vertex of the fan of rays,



FAN BEAM GEOMETRY

FIGURE 1. Fan beam geometry, including rotational motion characteristic of third generation scanners. The two dimensional matrix depicts the grid of pixels (elements of area) used for the reconstruction.

which intersect the arc of motion of the source. Ray spacing is set by the increment of displacement of the source along the arc. For reasonable object and system sizes, the individual detector must include a wide angle of acceptance of source photons within the scanning plane, on the order of 30 deg or more. For industrial scanning, such a requirement implies limitations or difficulties in collimation, and shielding, depending on the need for spatial resolution and freedom from scattering effects.

In addition to choice of source and geometry, options are also available as to individual and mode of electronic recording of the data. In the medical field, the method of current integration has been used exclusively, either in conjunction with scintillators or a gas ionization system. The current measured consists of photo-multiplier (PMT) output coupled to scintillators or the ionization current produced in the gas. More recently, Scientific Measurement Systems, Inc., (SMS) has developed a photon-counting or pulse-counting detection system, which has been successfully used in the scanning of a wide variety of industrial objects (Ref. 1). It employs a photo-multiplier coupled to a plastic scintillator, which emits light rapidly, within a few ns, following excitation. The pulse output is then processed through an amplifier-discriminator and recorded as a count in a scaler. Each approach has certain advantages and disadvantages where the scanning of industrial objects is concerned, depending on the specific configuration involved. These will be discussed briefly in the concluding section of this report.

Most all of the computer simulations and empirical measurements presented in this report were based on the TG geometry. This approach was due to the utilization of existing software and hardware at SMS and the valid candidacy of TG scanning for cylindrically symmetric objects, such as rocket

motors. However, most of the conclusions drawn are valid to a large extent for any system, as will be discussed specifically where appropriate.

The interplay between possible sources, objects of interest, detection methods, scanning configurations, resolution requirements, and reconstruction algorithms is multi-dimensional and highly variable. In order to assess in detail the optimum approach for scanning a certain object, a specific study must be made with definite goals as to capability, speed, and cost of the system. The primary intent in this report is to investigate in general the effects of beam-hardening and scattering on tomographic data and methods for measuring and correcting for them. Both phenomena will be present to some degree in any system. A secondary goal was to draw conclusions where possible about specific geometries and methods. Final choices of approach for a particular situation would require further design assessment within a more limited framework.

II. THEORETICAL AND EMPIRICAL CONSIDERATIONS

1. SPECTRAL CONSIDERATIONS

a. Photon-matter interactions -- A discussion of alteration of the spectral features of a photon flux as it penetrates through matter, known as beam-hardening in tomography, begins with a description of photon-matter interactions. Assume for the moment the following conditions: a) mono-energetic source, b) point source, c) point detector, d) homogeneous object, and e) perfect detection of each photon. For a beam of photons of intensity I , passing through a material of thickness x , with a linear absorption coefficient of μ , it is well known the transmitted intensity becomes

$$T = I e^{-\mu x} \quad (1)$$

This is a result of the change in intensity, which is directly proportional to the incident intensity and the thickness of the material. The quantity is termed the linear attenuation coefficient.

There are numerous physical processes through which the photon beam may be attenuated (Ref. 2). In practice, there are three principal interactions which are significant over different ranges of photon energies:

(1) photoelectric capture (.01 MeV - .5 MeV), (2) Compton scattering (.05 MeV - 10 MeV), and (3) pair production (1.02 MeV and up).

Photoelectric Effect: The Photoelectric Effect refers to the capture of a photon by a bound electron. All of the photon's energy is transferred to the electron, which breaks free of the atom. It then loses its energy (original-(electron binding)) in nearby matter and is recaptured by some other atom. The maximum photoelectric capture cross section for a given shell occurs at photon energies slightly greater than that shell's binding energy. For the same shell, increasing the photon energy leads to a dramatically decreasing capture coefficient, as can be seen in Fig. 2.

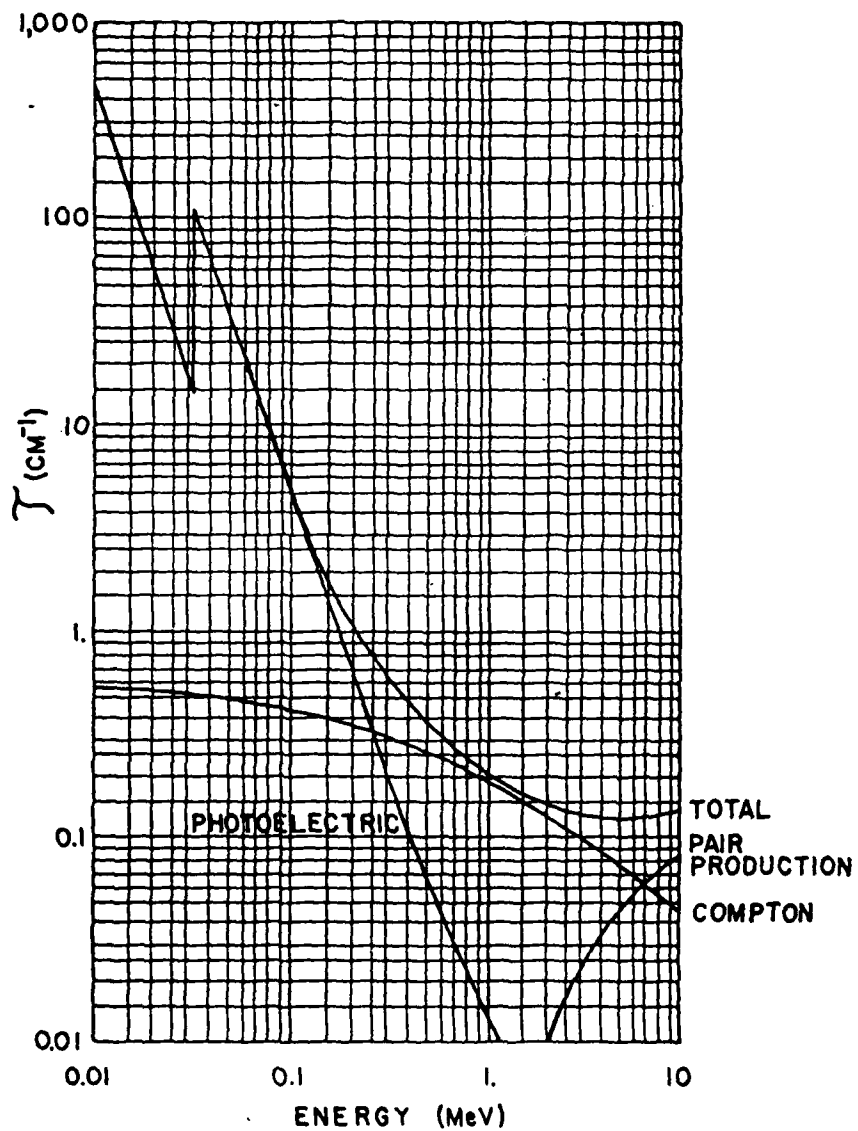


FIGURE 2. Photon attenuation coefficients in NaI, showing total absorption and fractional components due to Compton scattering, photoelectric absorption, and pair production. Data from Reference 3.

The major factors affecting photoelectric capture cross section include the number of electrons, the shell binding energies, photon energies and the presence of a strong electrical field. The general effect produced by these factors may be summarized by the following relations (Ref. 2):

$$\mu_{PE} \approx K Z^{4.5} / E^3 \quad (2)$$

$$1 < Z < 92$$

$$K \approx 3 \text{ for } 0.01 \text{ MeV} < E < 0.5 \text{ MeV}$$

$$K \approx 5 \text{ for } 0.5 \text{ MeV} < E < 2.0 \text{ MeV}$$

Compton Effect: Compton scattering refers to the deflection of a photon from its original path due to interaction with a "free" electron. During this process (also known as incoherent or inelastic scattering), part of the energy is transferred from the photon to the electron. The Compton electron recoils after breaking free from the atom, and subsequently loses its energy in nearby matter until it is recaptured. "Free" electrons are considered to be any electron in which the shell binding energies are small compared to the incident photon energies. In fact, for sufficiently high energies, even inner shells contribute significantly to the total capture cross section.

The principal theory in this area has been advanced by Klein and Nishina (Ref. 4) and is presented in detail in the following section on scattering. The Compton scattering coefficient is maximum at very low photon energies (.01 MeV), with the coefficients gradually decreasing with increasing photon energies (see Fig. 2).

The major factors affecting the Compton cross section are photon energy and the number of electrons. The general effect may be summarized by

$$\mu_c \propto Z f(E) \quad (3)$$

where $f(E)$ is a monotonic, gradual function of E .

Nuclear Pair Production: Pair production occurs at energies greater than 1.022 MeV. A photon disappears in the field of a nucleus, and a positron-electron pair is created. The electron is a "free" electron and is absorbed in nearby matter. The positron loses energy through atomic collisions and forms a "positronium atom". This atom then annihilates, creating two .511 MeV photons traveling in opposite directions.

For photon energies under consideration ($\sim 0.1-2.0$ MeV), the nuclear pair production cross section represents at most a few percent of the total attenuation coefficient in the objects of interest. For photon energies of even greater energy, more careful consideration would have to be given to that process, governed by the approximate dependence,

$$\mu_{pp} \propto Z^2 q(E) \quad (4)$$

where the energy-dependent $q(E)$ factor can be adequately described over limited intervals of range of energy.

In summarizing the three processes, the linear attenuation coefficient is given by

$$\mu_{total} = (\rho N_A / A) (\mu_{PE} + \mu_C + \mu_{PP}) \quad (5)$$

where ρ is the density in units of g/cc, N_A is Avogadro's Number, and A the atomic weight.

The mass absorption coefficient, μ_m , is μ_{total} / ρ . It is this coefficient that is usually found in tabular form.

Several general points are worth noting. For the energies under consideration ($\lesssim 2.0$ MeV), photoelectric and Compton are the dominant processes. Pair production would become important for photon flux with energies up to 6-12 MeV, as would be produced by an electron accelerator used to penetrate very massive objects. For the specific cases of solid propellant rocket motors, with only a very small fraction of mass with high atomic number, it is reasonable to neglect pair production even up to 6 MeV.

b. Extraction of densities from attenuation -- Most photon sources are polychromatic, i.e., they produce a variety of energies. With a few exceptions, isotopic sources emit a number of discrete x-ray energies. Electron accelerators or x-ray tubes produce the continuous bremsstrahlung spectrum characteristic of emission resulting from the de-acceleration of energetic electrons, with an end-point energy equal to the initial maximum electron energy. Examples of typical isotopic and bremsstrahlung spectra are presented in Table 1 and Fig. 3, respectively.

As discussed above, the linear attenuation coefficient varies substantially as a function of photon energy, as well as elemental composition. Neglecting pair production, the coefficient may be approximated by,

$$\mu(x, E) = \rho_d(x) \left[K_{PE} Z^{3.5} / E^3 + K_C f(E) \right] \quad (6)$$

with the transmitted photon strength by

$$I(x, E) = I(x_0, E) e^{-\int_{x_0}^x \mu(t, E) dt} \quad (7)$$

Ignoring the problems introduced by finite aperture considerations, and leaving out energy discrimination at the detection stage, the above equation may be rewritten,

$$\int_0^{E_{max}} I(x, E) dE = \int_0^{E_{max}} I(x_0, E) e^{-\int_{x_0}^x \mu(t, E) dt} dE \quad (8)$$

What is desired is to produce an electron density from

In the case of a single energy, a simple relationship is derived for the opacity M,

$$M = \int_{x_0}^x \mu(t, E) dt = -\ln \{ I(x) / I(x_0) \} = \int_{x_0}^x \rho_d(t) \left\{ K_{PE} Z^{3.5}(t) / E^3 + K_C f(E) \right\} dt \quad (9)$$

TABLE 1. Isotopic X-Ray Sources

Source (lifetime)	Form (Density) (gm/cm ³)	Energies (keV)	Abundances (%)	Attenuation Lengths ^a				
				Graphite (cm)	Aluminum (cm)	Iron (cm)	Tin (cm)	Lead (cm)
¹⁹² _{Ir} (74 days)	Ir metal (22.48)	310 ^b	146.9	4.15	3.56	1.15	0.83	0.22
		468	49.7	5.10	4.39	1.51	1.45	0.55
		610 ^b	18.1	5.56	4.81	1.67	1.69	0.71
¹³⁷ _{Cs} (30 years)	Cs ₂ O (4.25)	662	85	5.77	4.94	1.72	1.78	0.78
⁶⁰ _{Co} (5.3 years)	Co metal (8.9)	1173	100	7.87	6.28	2.39	2.75	1.53
		1332	100					

^aCalculated, using attenuation coefficients from Reference 2. An attenuation length is the thickness of material that will scatter or absorb 63.2% of the incident photons.

^bAverage energy of a cluster of lines.

^cAbundances are averages per disintegration (1 Curie = 3.7×10^{10} disintegrations/sec).

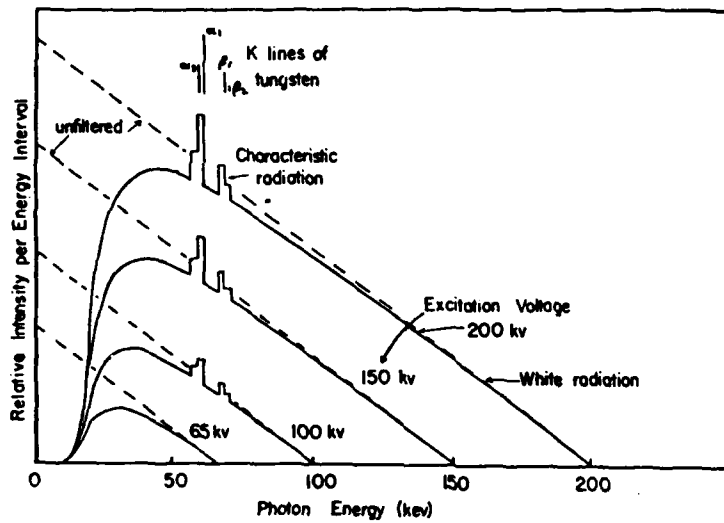


FIGURE 3. Bremsstrahlung spectra produced with a tungsten anode and voltages of 0-200KV. Taken from Reference 5.

Because of the dependence of the photoelectric term on Z , an effective way would be needed in order to produce an estimate of the total number of electrons. For an object composed of a single material, either of one element or a known homogeneous mixture of several elements, the relationship in Equation (7) can be fully accounted for by computing values of the right hand side of Equation (9) for various thicknesses of material. A conversion table or a fitted function can then be used to map measured values to true values.

For materials containing several different elements in unknown mixture or distribution within the object, different techniques may be used for ascertaining densities along specific ray paths through the object. For example, an estimate can be made of an effective Z value in order to account for the photoelectric term. Subsequent use of the initial image to estimate composition distribution and generate a second, corrected image is a possibility.

An even simpler situation arises where the photoelectric term can also be neglected, and a direct Compton normalization provides a unique map between electron density and measured transmission values. For simulated and measured cases presented in detail in the remainder of this report, that approach is a valid one and has been used extensively.

For the ideal case where transmission of at least two energies are available, individual photoelectric and Compton tomograms may be produced.

Decomposition of the data is given by the following relationships:

$$\ln \{ I(E_1) / I_0(E_1) \} = A/E_1^3 + B f(E_1) \quad (10)$$

$$\ln \{ I(E_2) / I_0(E_2) \} = A/E_2^3 + B f(E_2) \quad (11)$$

Maps or tomograms of the quantities A and B may be obtained, where

$$A = \int_{\lambda_0}^{\lambda} e_d(t) K_{PE} Z^{3.5}(t) dt \quad (12)$$

$$B = \int_{\lambda_0}^{\lambda} e_d(t) dt \quad (13)$$

A pixel by pixel correlation between the two tomograms yields values of atomic number Z and electron density e_d .

This approach, known as two-energy tomography, requires sufficient sensitivity with at least one source photon energy through an appreciable photoelectric magnitude. Consequently, two different sources have to be utilized. A second scan creates problems of registration between tomograms and requires additional time for data acquisition and processing. An alternative is the use of a single polychromatic source in conjunction with energy discrimination. Discrimination can be accomplished either by selective filtration of the flux by windowing an energy interval in the recorded detector pulse height spectrum. Such gating requires adequate energy resolution in the detector system and the capability of upper and lower discriminator levels as found in pulse-counting systems.

No further attention has been given to the two-energy technique in this report for two reasons. Most importantly, the detection of features as investigated in this report requires primarily the location and imaging of flaws, rather than accurate measurement of elemental and electron densities. Secondly, the successful application of two-energy tomography in the inspection of aerospace components would require a more specific research effort, particularly in the area of hardware development. Accordingly, it is beyond the scope of work here.

c. Beam hardening -- The term "beam hardening" refers to the preferential attenuation of the lower energy photons in a polychromatic source

spectrum as the photon flux penetrates matter. This phenomenon arises because of the energy dependence of the attenuation coefficients as depicted in Fig. 2. The energy spectrum of the flux is changed in a non-linear fashion along a particular ray path. The beam flux is hardened in the sense that the altered spectrum is more penetrating, increasingly so as the degree of alteration progresses. Relationships governing this interaction are more complicated than for the simplified one-energy case described above.

For an arbitrary initial spectral distribution $I(X, E)$ with no energy discrimination in detection, the general equation for transmission obtained from combining Equations (8) and (9) is,

$$T = \int_0^{E_{\max}} I(X_0, E) e^{-\int_{X_0}^X \mu_d(t) \{K_{PE} \frac{z^2(t)}{E^3} + K_c f(E)\} dt} dE \quad (14)$$

It is desirable to produce a quantity that again corresponds to the total number of electrons. Note that now the logarithm does not directly yield the value sought,

$$M = -\ln \left[\frac{\int_0^{E_{\max}} \int_{X_0}^X I(X_0, E) e^{-\int_{X_0}^X \mu_d(t, E) dt} dE}{\int_0^{E_{\max}} I(X_0, E) dE} \right] \quad (15)$$

but rather an intensity-weighted, energy-averaged total attenuation,

$$M = -\ln \int_0^{E_{\max}} \left\{ A(X, E) e^{-\int_{X_0}^X \mu_d(t) K_{PE} \frac{z^2(t)}{E^3} dt} - f(E) \int_{X_0}^X \mu_d(t) dt \right\} dE \quad (16)$$

where $A(X, E) = I(X, E) / \int_0^{E_{\max}} I(X_0, E) dE$, and the desired quantity

is $B = \int_{X_0}^X \mu_d(t) dt$. If the assumption is made that Equation 16 may be approximated by a polynomial in the symbol B, then

$$a_1 B + a_2 B^2 + \dots = -\ln \int_0^{E_{\max}} \left\{ \right\} dE = C \quad (17)$$

Mathematical techniques similar to those used in Reference 6 may be used to find constants a_i , and subsequently

$$B = \alpha_i (C + \alpha_2 C^2 + \alpha_3 C^3 + \dots) \quad (18)$$

where the α_i are found from the a_i . The end result of this technique is to analytically describe the coefficients α_i , and to relate them mathematically to statistical quantities from Equation (16).

To correct averaging effects where composition is known, a simple method is to generate a table according to Equation (16) and to fit it with a polynomial similarly to Equation (18). This type of correction can be accomplished empirically by employing a set of uniformly thick attenuators to measure deviation from linearity of signal strength as a function of total mass penetrated. In addition to accounting for the dependence of detector response upon count rate and other nonlinear effects such as erroneous signal from scattering, this procedure corrects for beam hardening. Ideally, the attenuators used are identical in composition to the object. An empirical correction is referred to as a mass calibration series.

As is implied by the energy dependence of the attenuation coefficients exhibited in Fig. 2, beam hardening efforts are more dramatic where photoelectric contributions to attenuation are appreciable. Presented in Table 2 are initial and final average spectral energies for a selection of combinations of bremsstrahlung end-point and total mass penetrated. The composition was assumed to be carbonaceous and the density to be 1.7 g/cc. The initial bremsstrahlung spectrum in each case was taken to be the linear thick target yield (Ref. 5),

$$I(E) = D(E_m - E) \quad (19)$$

TABLE 2. Transmission and Beam Hardening
of Bremstrahlung Spectra

Thickness of Carbonaceous Material (CM)	13		26		45		75	
	I ^c	II ^d	I	II	I	II	I	II
150 (50) T(%) ^a $\frac{E_f}{E_i}$ ^b	1.6	0.25	0.047	0.097				
	80.7	107.8	91.2	110.9				
300 (100) T(%) $\frac{E_f}{E_i}$	3.3	1.4	0.17	0.08				
	150.5	183.0	175.5	196.1				
700 (233) T(%) $\frac{E_f}{E_i}$	7.2	4.5	0.74	0.51	0.034	0.024	0.00036	0.00026
	340.2	371.7	402.7	418.2	462.7	469.5	519.0	522.1
1000 (333) T(%) $\frac{E_f}{E_i}$	9.7	6.7	1.3	0.96	0.091	0.068	0.0018	0.0013
	480.7	512.8	568.5	584.3	652.1	659.9	731.3	735.53
2000 (667) T(%) $\frac{E_f}{E_i}$			3.7	2.9	0.50	0.41	0.028	0.023
			1099.5	1122.4	1256.6	1270.4	1410.1	1419.2
3000 (1000) T(%) $\frac{E_f}{E_i}$			6.2	5.2	1.2	1.0	0.11	0.096
			1608.1	1639.2	1833.1	1853.1	2059.2	2071.6
6000 (2000) T(%) $\frac{E_f}{E_i}$							0.51	0.45
							3290.4	3310.4

^aT is the transmission value in percent

^b $\frac{E_f}{E_i}$ is the average final energy after transmission, to be compared to the average initial energy (= E / 3).

^cCase I simulates the carbonaceous material.

^dCase II simulates 5 mm of steel as well as the carbonaceous material.

where D is a constant and E_m is the end-point energy.

Transmission values were calculated for a grid of 200 energy values regularly spaced over the full range. The average energy \bar{E} is defined as

$$\bar{E} = \frac{\sum_{i=1}^m E_i I(E_i) T(E_i)}{\sum_{i=1}^m I(E_i) T(E_i)} \quad (20)$$

where the transmission values $T(E_i)$ were calculated explicitly according to Equation (16).

The trend toward more severe hardening for lower energies and composition of higher atomic number Z is evident. The implication of the results in Table 2 for tomographic inspection of largely carbonaceous solid propellant rocket motors is minimal ambiguity due to hardening.

Examples of second order polynomial fits to calculated trans-attenuation lengths are shown in Table 3. The extracted coefficients and those from several other cases are presented in Table 4. The fits were obtained according to Equation (16) for ^{192}Ir , ^{60}Co , and various bremsstrahlung sources. The material penetrated was again taken to be carbonaceous with a density of 1.7 g/cc. The actual and fitted values are represented in Table 3 in units of cm of the material.

The quality of the fits for the isotopic sources is excellent. The lack of any low energy components, which would lead to increased beam hardening, facilitates the agreement. The fits for the bremsstrahlung sources are also accurate, except for the very low mass region where the hardening of the beam is significant. The use of a third order polynomial improves the fit only slightly. The rapidly changing nature of the mass-versus-attenuation function at the low end calls for a segmenting of the attenuation

TABLE 3. Empirical Fits to the Mass-versus-Attenuation Function in Carbonaceous Material

Photon Source	Transmission (%)	Displacement (cm)	FIT	DIFF. (%)	Attenuation Length
150 kV Bremstrahlung	82.40331	0.20	0.52	-156.04	0.19
	20.85431	4.23	4.43	-4.80	1.57
	6.33317	8.25	8.18	0.78	2.76
	2.01363	12.27	12.11	1.29	3.91
	0.65769	16.30	16.25	0.27	5.02
300 kV Bremstrahlung	87.32525	0.25	0.47	-85.28	0.14
	21.92701	5.32	5.47	-2.90	1.52
	6.27760	10.38	10.34	0.38	2.77
	1.88578	15.44	15.33	0.73	3.97
	0.58565	20.50	20.47	0.16	5.14
^{192}Ir	91.76628	0.51	0.50	0.36	0.09
	16.66610	10.62	10.60	0.14	1.79
	3.10753	20.73	20.72	0.01	3.47
	0.59646	30.84	30.85	-0.04	5.12
	0.11803	40.95	40.95	-0.02	6.74
^{60}Co	93.11063	0.73	0.73	0.00	0.07
	22.35992	15.42	15.42	0.00	1.50
	5.38100	30.11	30.11	0.00	2.92
	1.29769	44.79	44.79	0.00	4.34
	0.31361	59.48	59.48	0.00	5.76

TABLE 4. Coefficients^a of Fits to Mass Functions for
Bremstrahlung Spectra and Isotopic Sources

Endpoint Energy (KV)	Carbonaceous Material		Steel	
	B	C	B	C
150	2.639	0.119	0.127	0.032
300	3.446	0.104	0.400	0.053
700	4.620	0.134	--	--
1000	5.192	0.184	--	--
2000	6.972	0.282	--	--
3000	8.287	0.417	--	--
192 I _r	5.859	0.032	1.315	0.010
60 Co	10.286	0.005	--	--

^aB and C are the second and third coefficients in a polynomial fit of the type $BX+CX^2$ where X is the attenuation length.

range. Limited segments could then be fit individually much more accurately than the entire range is with a single function. Functions other than polynomials could also be used. The fits improve as the end-point energy is raised, which is an indication that the hardening is not as severe.

A correction of this type can be done for any material of known, homogeneous composition. Fits to steel as a medium have yielded results similar to those reported here for carbon, as is shown for the lower energy sources in Table 4. In effect, this correction is one of several folded into the mass calibration procedure discussed above. Where possible, that empirical procedure is the most direct way in which to correct the data.

In any case, in situations where noticeable artifacts are generated due to beam hardening, adequate corrections can easily be made. In a large number of applications, including scanning of rocket motors, the effect of the phenomenon is sufficiently slight as not to seriously impede detection of flaws and other high contrast density variations.

The effect of beam hardening is to overestimate true signal strength and thereby underestimate opacity. Any other process which inflates apparent signal similarly depresses opacity and leads to an underestimate of mass in the tomogram. The detection of scattered photons is perhaps the most dominant of these.

2. SCATTERING EFFECTS

a. Scattering Processes -- The Compton scattering of photons by electrons is one of the most prevalent phenomena occurring in a system utilizing the higher energy photons necessary for the tomographic scanning of dense objects. For photon energies in the range of several hundred keV (tens of keV for low Z materials) to several MeV, that process is primarily responsible for the flux attenuation in the object. Upon emerging from the object after

single or multiple scattering, the scattered photons may enter detectors other than the ones encompassing their initial trajectories and register incorrectly as transmitted flux along an alternate ray path. Depending upon the composition of scintillator, the detection process at high energies includes Compton events in the detector or plastic scintillator. Compton scattering produces energetic electrons which, in turn, excite light emitting atomic and molecular states. Finally, the photons scattered in the detectors and surrounding structural or shielding material in the detector bank may interact in other detectors and produce counts which are not associated with the directly transmitted flux.

The relative importance of Compton scattering versus photoelectric absorption, in which the photon is eliminated and a photoelectron is produced, depends upon the specific photon energy and Z value of the medium. In general, the photoelectric cross section decreases rapidly with increasing photon energy and increases dramatically with increasing Z . The Compton cross section is more gradual as is apparent from Fig. 2 and Equations (2) and (3). Even for an initial photon energy where Compton predominates in the interaction, multiple scattering of the photon can lead eventually to a reduced energy where photoabsorption will occur. For very high Z materials, such as lead, photoelectric absorption is significant for photons up to several hundred keV in energy.

Two facets of the Compton process must be kept in mind when one is attempting to gauge the scattering. The first, the angular distribution of the scattered photons, is given by a simple expression,

$$\frac{d\sigma}{d\Omega} = C \frac{(1 + \cos^2\theta)}{1 + (1 - \cos\theta)^2} \left[1 + \frac{\gamma^2 (1 - \cos\theta)^2}{(1 + \cos^2\theta)(1 + \gamma(1 - \cos\theta))} \right] \quad (21)$$

where C is a constant, θ is the angle of scatter with respect to the incident direction, and $\gamma = E/511$ keV, where E is the incident energy of the photon in keV. The energy E' of the scattered photon is given by

$$E' = \frac{E}{1 + (1 - \cos \theta)} \quad (22)$$

For the energies discussed in this report, the differential cross section $\frac{d\sigma}{d\Omega}$ is substantially forward peaked, as shown in Fig. 4.

The fraction of energy lost by the photon in each collision depends upon the angle. The mean energies given a recoil Compton electron in a single collision are 87 keV, 164 keV and 232 keV by the 310 keV, 468 keV and 610 keV lines, (or clusters of lines), respectively, emitted by an ^{192}Ir source. The maximum energies are shown in Fig. 5. Sufficient losses in energy due to multiple scattering can eventually lower the photon energy to a value where photoabsorption will occur.

The assessment of the scattering in a given situation is much simpler to accomplish by empirical measurement than by computer simulation. As the scattering and transmission patterns are very much dependent upon source and object, most related information available is in the form of measurements reported for specific cases. Industrial radiography is the one area where some idea can be obtained of the magnitude of the effects to be encountered in tomography, since source energies and objects are often similar.

One such industrial measurement is presented in Fig. 6, for flat steel plates penetrated by bremsstrahlung fluxes with four different end-point energies. At fairly low projection densities (15g/cm^2), the scattering becomes comparable to and greater than the recorded direct transmission.

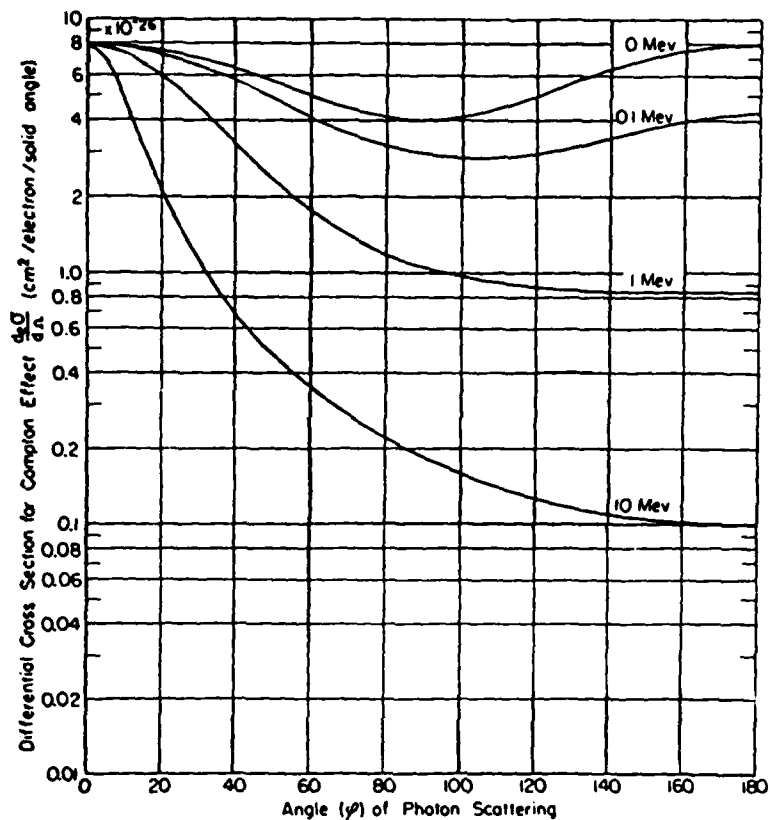


FIGURE 4. Graph displaying the Compton scattering differential cross section as a function of photon scattering angle and photon energies of 0, 0.1 MeV (100 keV), 1.0 MeV (1000 keV), and 10.0 MeV (10,000 keV). Taken from Reference 5.

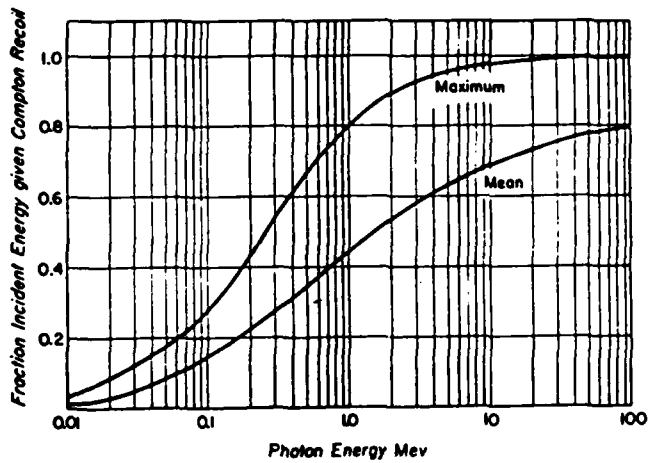


FIGURE 5. Graph of maximum and minimum energy imported to Compton recoil electron as a function of photon energy. Taken from Reference 5.

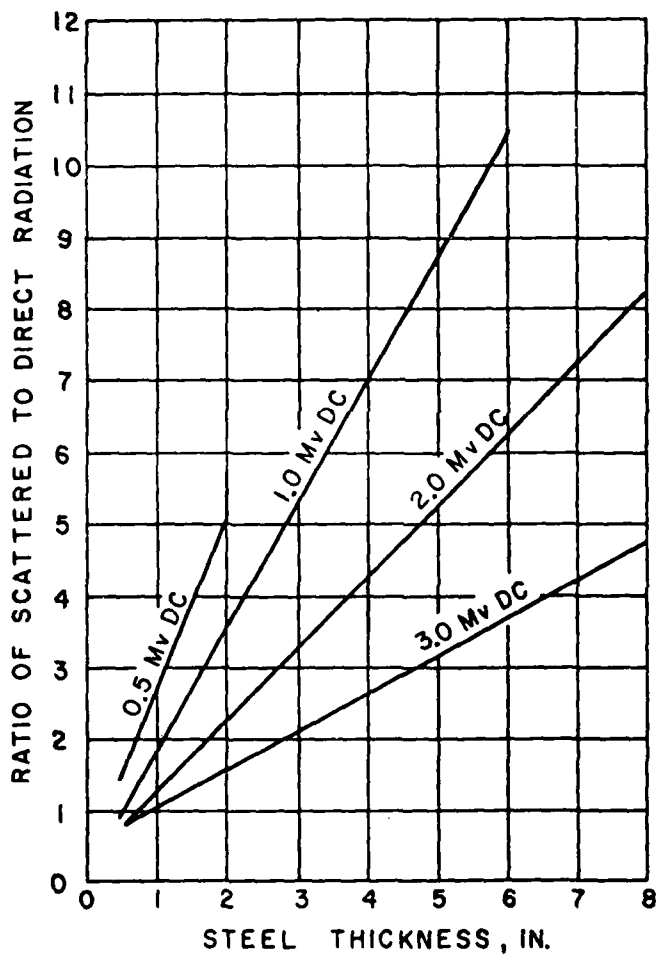


FIGURE 6. Ratios of scattered to direct radiation for bremsstrahlung spectra penetrating steel, as a function of endpoint energy and thickness of steel. Taken from Reference 7.

Two factors imply that tomography would have greatly reduced susceptibility to interference from scattering for a case as in Fig. 6. The first is the inherent use of collimation of source and detectors in the tomographic system. The second is the use of scintillation detectors, where the probabilities of detection of the scattered photons (with variously reduced energies) should be comparable to those for transmitted photons. This is in contrast to the preferential sensitivity of radiographic film to scattered photons. Nevertheless, it is clear that such effects should be carefully estimated or measured in tomographic systems as well.

It is obviously desirable that some method be available for making qualitative and, if possible, quantitative predictions of the degree of scattering expected for a proposed scanning configuration and object. In situations where several attenuation lengths of material are encountered by a photon along a particular ray path, it is very difficult to determine analytically the final scattered angular distribution. Direct integration of an extended flux transmitting through a three dimensional object, with successful scattering governed by Equations (21) and (22), is practically impossible to model, given a finite amount of computer time. There is a viable alternative, which has been used for years in a wide variety of radiation transport studies. It is the use of a Monte Carlo code, whereby a set of probabilistic events are tabulated according to random selection.

b. Scattering Simulations: Monte Carlo code -- The Monte Carlo scattering program TOMOS, created by Scientific Measurement Systems, Inc., has been used to obtain estimates of the interdetector scatter and object scatter expected for several different tomographic systems. The simulated geometry is the fan beam configuration, which is appropriate for SG or TG scanners. A schematic of the system is shown in Fig. 7, with key geometric parameters listed.

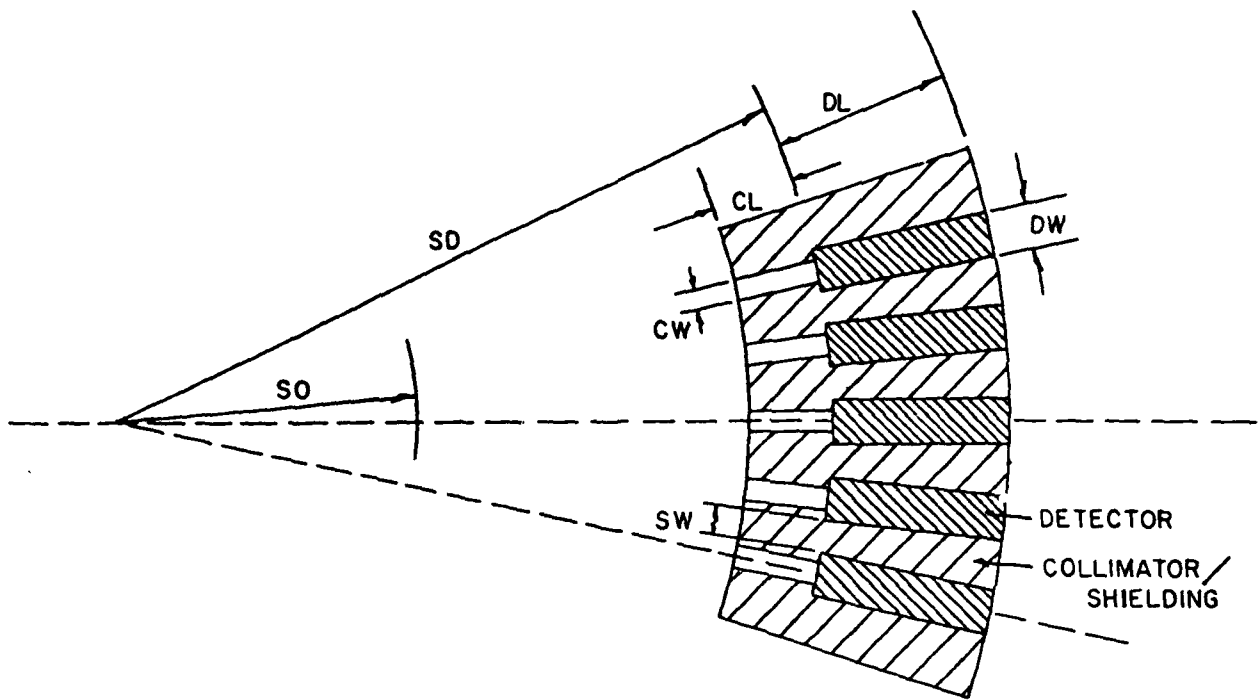


FIGURE 7a. Cross-sectional top view of geometry of tomographic system simulated in the computer code TOMOS.

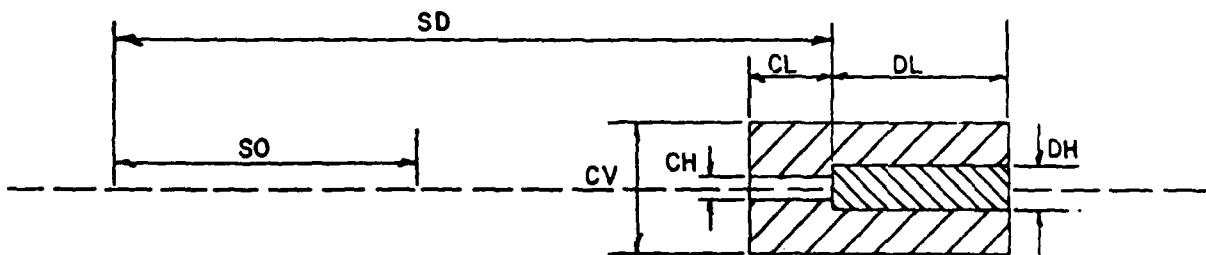


FIGURE 7b. Cross-sectional side view of same system.

Parameters:

- | | |
|--------------------------------------|--|
| 1. SO: Source-object distance | 6. SW: Spacing width |
| 2. SD: Source-detector distance | 7. CW: Collimation (aperture width) |
| 3. DW: Detector width | 8. CL: Collimation length |
| 4. DL: Detector length | 9. CH (See Fig. 1b): Collimation height |
| 5. DH (See Fig. 1b): Detector height | 10. CV (See Fig. 1b): Collimator/shield height |

Collimation and shielding of the rectangular detectors is represented by a single jacket of material, which encloses them except for the rear faces. The front and rear surface of the detectors are defined as arcs of circles described by radii of lengths equal to the distances from the source to the front and back of the detector, respectively, with center at the source. The four lateral surfaces are pairs of parallel planes. For the geometries under consideration in this report, such a volume very nearly approximates a rectangle.

In the scanning geometry, the center of the object is normally located halfway between source and detector but can be varied in position. The object may consist of a cylinder, or a rectangle, of homogeneous density. The simplicity of the system minimizes computation time, while providing information about basic geometries. From these results, inferences can be drawn about a variety of systems. The solid angle and direction of the beam flux is specified.

The processes leading to beam attenuation are taken to be photoabsorption and Compton scattering. Pair production is neglected for energies of photons up to several MeV. The beam can be described by several line components, with energies and relative strengths specified.

Operationally, a photon is emitted from the source and tracked through the object and/or detector bank until it is (1) photoabsorbed, (2) escaped from the object and missed the detector bank, or (3) escaped from the detector bank. Backscattering to the object was neglected. The initial direction of the photon, limited to those within the specified solid angle, is chosen randomly. The occurrence of attenuation is also determined randomly, according to the coefficients defined in Equations (2) and (3). For Compton scattering events, the angle of scattering is chosen randomly

according to the differential cross section expressed in Equation (21) and the assumption of randomness in azimuthal angle. The scattered photon energy is adjusted according to Equation (22).

The detection of a transmitted or scattered photon in one detector is counted if any interaction takes place within that volume. The effects of energy discrimination as used in the pulse-counting mode have been neglected, as has the effect of energy deposition in a current integration system.

An example of a comparison between TOMOS predictions and measurements is presented in Table 5. It consists of interdetector scattering coefficients for a previous version of the SMS tomographic detector assembly and an ^{192}Ir source flux. The SMS assembly is of the configuration shown in Fig. 7, with 31 individual scintillation detectors.

The following geometrical parameters were used in the simulation:

SD = 122.0 cm	SW = 7.8 mm
SO = 61.0 cm	CW = 2.4 mm
DW = 6.4 mm	CL = 75.0 mm
DL = 200 mm or 125 mm (to cover the range of actual lengths)	CH = 2.0 mm
DH = 20 mm	CV = 38.1 mm

The front collimator material was lead, and the spacing material was delrin. As the scintillators comprise a group of several different shapes and lengths, two different lengths were simulated in order to provide a range of values.

For the simulation, the solid angle of the incident flux was limited to that which included the aperture opening of the center detector. Counts in neighboring detectors were recorded and converted to percentages of the detected counts in the primary detector. For the case of equal detector efficiencies, those percentages are then equivalent to percentages of the signal strength in a given detector due to scattering from neighboring detectors, or interdetector scattering coefficients. The lead collimator was treated as opaque to minimize computer time required in the simulation.

TABLE 5. Interdetector Scattering Coefficients^a
for SMS Tomographic System

(Ratio of Scattered Counts to Direct Counts)

N ^b	Simulated				Experimental			
	C ₃₁₀	C ₄₆₈	C ₆₁₀	C _T	Detector A (%)	Detector B (%)	Detector C (%)	Detector D (%)
DL = 20.0 cm								
1	2.45	2.32	2.14	2.40	1.212	1.568	1.633	1.99
2	1.08	0.98	0.91	1.04	0.525	0.723	0.391	0.69
3	0.52	0.50	0.46	0.51	0.302	0.211	0.344	0.44
4	0.29	0.25	0.31	0.28	0.094	0.201	0.183	0.30
5	0.13	0.18	0.16	0.14	0.094	0.117	0.091	0.30
6	0.093	0.12	0.091	0.099	0.051	0.056	0.076	0.14
7	0.088	0.073	0.062	0.083	0.027	0.050	0.054	-
8	0.043	0.068	0.050	0.049	0.031	0.036	-	-
DL = 12.5 cm								
1	2.36	2.06	2.14	2.28				
2	0.87	0.83	0.76	0.85				
3	0.45	0.42	0.42	0.44				
4	0.26	0.26	0.19	0.26				
5	0.11	0.095	0.19	0.11				
6	0.090	0.085	0.050	0.086				
7	0.075	0.040	0.045	0.065				
8	0.040	0.040	0.035	0.040				

^a Lowest statistical accuracy was 30% for the N = 8 case.

^b N is the relative order of the detector on either side of the scattering detector.

^c DL denotes detector length.

The results of the simulation are shown in Table 5 for individual photon lines and the composite results for both lengths of detectors. Since the scattering for this situation is symmetric, the data for corresponding neighboring detectors on either side of the primary detector were averaged. As seen in the table, the scatter coefficients are fairly insensitive to detector length (from 100 mm - 200 mm), and the contributions from the different lines are comparable.

A measurement of the response of the SMS system was performed using a 24 Curie ^{192}Ir source. All apertures, except for the center detector, were shielded with 10 cm thick lead. The values are fairly close to the Monte Carlo values. It should be expected that the simulation would yield somewhat higher values due to the fact that some energy discrimination is exercised, which would preferentially reject the pulses generated by the lower energy, scattered photons.

The variation between different detectors presumably arises from different physical shapes and the dependence upon phototube gain and the discriminator threshold. In fact, the normalization value, which is the detection efficiency of the primary flux, varies as much as 20 to 30 percent for different lengths. While simulations can provide qualitative information, it is apparent that specific corrections to data should be based on careful and frequent measurements of the scattering in each particular tomographic system.

3. SCATTERING SIMULATIONS

a. Object scattering -- In order to make a qualitative assessment of the magnitude of object scattering effects expected for the scanning of the essentially cylindrically symmetric geometry of rocket motors, a series of simulations have been carried out with TOMOS for cylinders of homogeneous

density. The configuration simulated is depicted in Fig. 7. The cylinders, including outer diameters of 13 cm, 25 cm, 45 cm and 75 cm, were each assigned a density of 1.7 g/cc and assumed to be carbonaceous material. The small amounts of metal casing and propellant liners present in a typical cross section of a rocket motor were neglected. The internal cavity, which varies substantially from motor to motor and also longitudinally within a given motor, was also neglected.

- Single energies for the source photons were used in each case, to allow a reasonable computation time for the Monte Carlo code. These were 300 keV for the two smaller diameters, 1250 keV for the 45 cm cylinder, and 2000 keV for the largest. These provided on-diameter transmission values of approximately 7 percent, 0.6 percent, 0.6 percent, and 0.15 percent, from smallest to largest cylinder. These energies correspond to those which are easily attainable from isotopic sources, high energy x-ray tubes, or electron accelerators.

The source detector distance was taken to be twice the object diameter in each configuration. A detector array of seven elements was treated as an opaque collector with individual detectors of cross sectional dimensions 2 cm x 1 cm placed contiguously on the source-detector arc. The detector assembly was centered on the source-object axis, where the ratio of fluxes of scattered to transmitted photons should be at a maximum. The center of the objects were halfway between source and detectors, except for Case II.

No collimation was employed in five of the examples. These results should be valid for FG scanning configurations as well as SG and TG scanners. As can be seen in Table 6, the geometries with no collimation can lead to appreciable amounts of object scattering, but the scattering exhibits a gradual dependence on detector location. The effect is one of lessening

TABLE 6. Monte Carlo Object Scattering Coefficients

S_n^a (n = order)	S_1	S_2	S_3	S_4
Configuration	(%)	(%)	(%)	(%)
I ^b	19	18	20	17
II ^c	5.8	8.9	9.0	13.1
III ^d	6.3	4.1	3.8	4.6
IV ^e	27	35	32	38
V ^f	17	20	16	22
VI ^g	68	55	60	55

^aThe coefficient S is the percentage contribution to total counts due to detection of photons scattered by the object.

^b13 cm diameter carbonaceous cylinder, 300 keV source photon energy, no collimation, 26 cm source-to-detector distance.

^cSame as Case I, except with source-to-detector distance of 39 cm (26 cm from object center to detector).

^dSame as Case I, except with collimation apertures of 8 mm width and 50 mm depth.

^e26 cm diameter carbonaceous cylinder, 300 keV source photon energy, no collimation, 52 cm source-to-detector distance.

^f45 cm diameter carbonaceous cylinder, 1250 keV source photon energy, no collimation, 90 cm source-to-detector distance.

^g75 cm diameter carbonaceous cylinder, 2000 keV source photon energy, no collimation, 150 cm source to detector distance.

apparent contrast in the projection data rather than generating noticeable artifacts, due to disparity in recorded signal strength in adjacent detectors. The cylindrical geometry is responsible for the gradual effect, being devoid of any long, straight, high density edges which would lead to a sharp discontinuity in the scattered to transmitted pattern.

The lesser effect associated with extended scanning geometries, such as in Case II, arises largely because of the increased distances between scattering points within the object and the detectors. The solid angle of the point-source emission was assumed, in each case, to be defined as that which just encompassed the diameter of the object, and measured the height of the detectors at the detector assembly. One exception was Case VI, for which the detectors were increased in size to 12 cm x 6 cm and the incident flux was constrained to that which intercepted the detectors. Collimation restricting the beam to such a fan-shaped volume would be appropriate to minimize out-of-slice-plane scattering contributions, from the object and the structural and shielding material at the detector assembly.

In cases where object scattering is appreciable, the choice of source-detector distance and detector collimation can minimize it. Table 6 includes cases of increased object-detector distance and detector collimation for the 13 cm diameter cylinder.

It should be pointed out that collimation to an effective area with dimensions on the order of mm is difficult to achieve in an FG configuration, where the detector must accept flux from a rotating source over a wide range of angles.

In addition to collimation, selective filtering of the transmitted flux with high Z materials, such as lead, can effectively eliminate scattered photons with substantially reduced energies, particularly where high energy

isotopic sources are used. This technique is widely used in industrial radiography to reduce fogging of film due to preferential detection of scattered photons. Such filtering would also attenuate the lower energy end of a bremsstrahlung source spectrum. This may or may not be detrimental, depending upon the source filtering and transmission characteristics of the particular system. The optimum filtration can easily be determined for a given configuration, either by simulation studies or measurement.

b. Interdetector scattering -- The scattering in a tomographic system which can be measured or estimated most accurately, and which is independent of the object being scanned, is the scattering of transmitted beam in a detector into neighboring detectors, where it may also be recorded. As described above, the magnitude of the process can be determined with confidence from simulation codes.

Several sets of such scattering coefficients have been calculated for a fan beam geometry, using TOMOS. The source simulated was ^{60}Co and the scintillation material was NE102. NE102 is the fast plastic utilized in the SMS photon counting detector system. The average energy for ^{60}Co of 1250 keV is also comparable to the higher energies in bremsstrahlung spectra appropriate for scanning the larger masses of objects discussed in this report. The shielding requirements should be substantially more severe than for lower energies.

The results presented here for scattering coefficients are overestimates, and hence, upper limits in both cases in that transmitted and scattered photons are counted if they interact in a scintillator at all. The actual scattered signal recorded, relative to the transmitted one, would be reduced due to the lower average energy of the scattered photons. In the pulse counting mode, pulse height discrimination allows preferential rejection

of lower amplitudes. In the current integration mode the contribution to the signal is directly proportional to the energy deposited, which may in some cases be less on the average for scattered photons than for the higher energy transmitted photons.

A restricted rectangular geometry was chosen for the cross section area of the scintillators, under the assumption that good spatial resolution (~ 2 mm) and an optimum transmitted-to-scattered ratio were desirable. In general, the area of the scintillator should be nearly equivalent to the effective detection area desired, since superfluous volume increases sensitivity to scattering without increasing detection of transmitted photons. Accordingly, cross sectional dimensions of 4 mm x 4 mm were used, with a depth of 150 mm.

Coefficients were tabulated for various detector spacings, with and without lead shielding in the volume between detectors. A source-to-detector distance of 122 cm was used for all cases. The results are shown in Table 7. The coefficients are represented as percentages of counts recorded in the center, primary detector. The quantity R_t is simply twice the sum of the coefficients and represents the total additional contribution to the signal in a given detector due to scattering from neighbors, where the primary and a sufficient number of neighboring detectors are equally illuminated.

Increasing space between detectors and inserting lead shielding greatly reduces the cross-talk between detectors. Ideally, high density packing of detector elements provides for maximum utilization of data acquisition time. The degree of packing feasible is obviously a function of beam energy and total object density. The same considerations apply for an FG design. Spacing detectors to allow for shielding implies some additional mechanical motion of the system and time to complete adequate ray sampling through the object.

TABLE 7. Calculated Interdetector Scattering Coefficients

Case I	IA	IIA	IIB	IIIA	IIIB	IVA	IVB
Coefficient (%)							
R1	100	100	100	100	100	100	100
R2	1.037	0.467	0.183	0.273	0.029	0.140	0.003
R3	0.459	0.194	0.044	0.111	0.005	0.059	0.001
R4	0.256	0.104	0.011	0.066	0.004	0.024	-
R5	0.168	0.065	0.005	0.043	-	-	-
R6	0.118	0.052	0.001	0.033	-	-	-
R7	0.095	0.026	0.001	0.015	-	-	-
R8	0.057	0.017	-	-	-	-	-
R9	0.053	0.017	-	-	-	-	-
RT	4.486	1.884	0.490	0.490	0.076	0.446	0.008

Cases:

- IA - No spacing, no shielding
- IIA - 4 mm spacing, no shielding
- IIB - 4 mm spacing, no shielding
- IIIA - 8 mm spacing, no shielding
- IIIB - 8 mm spacing, with lead
- IVA - 16 mm spacing, no shielding
- IVB - 16 mm spacing, with shielding

Alternatively, the use of little or no shielding may, or may not, require corrections for the cross talk between detectors. In certain high contrast situations, such as the detection of cracks within a homogeneous solid propellant, such corrections may not be necessary. However, where interfaces of media of high density contrast are involved, such as the detection of delamination between solid propellant and liner, corrections may be required for image clarity.

The effectiveness of the shielding configurations discussed here would be dramatically greater for source photons below 1.0 MeV in energy. The rapid increase in the photoelectric cross section in lead in that range would lead to more rapid absorption of the scattered photons. Similarly, a high Z detector, such as BGO ($\text{Bi}_4\text{Ge}_3\text{O}_{12}$), would afford shorter depths for adequate attenuation of the primary beam. BGO is commonly used in medical tomographs. The shorter depth coupled with the forward direction of the scattering would tend to reduce the coefficients. However, the high Z scintillator would be very efficient in absorbing the scattered photons. Obviously, a simulation for the specific geometry of interest would be needed.

III. SIMULATIONS OF A PHANTOM ROCKET MOTOR

1. MID-SECTION REGION

A series of computer simulations has been obtained for the mid-section of a solid propellant rocket motor with outer diameter of 45.7 cm. The simulation in each case included the generation of a complete set of projections for 400 views (angles) with a ray spacing of 1.0 mm at the center of the object. The source detector distance was set at 122 cm, using the fan beam geometry depicted in Fig. 7 with a fan angle of 44 deg. Initial simulations were done for a point source - point detector system. Reconstructions were accomplished with the SMS filtered-back projection algorithm.

The description of the phantom was as follows: the outermost component was taken to be a cylindrical steel shell of thickness 2.5 mm and density 7.86 g/cc. Internal to the steel was a 1.587 mm thick cylinder of cork, with density of 0.5 g/cc. Internal to the cork was situated a 1.5 g/cc carbon-aceous material with internal star-shaped cavity to approximate the solid propellant. The tips of the star cavity were represented in two dimensions by an axis cross section of paraboloids. The total number of equations used to describe all surfaces, including the six pointed star cavity and excluding flaws, was only 15.

The flaws placed in the phantom included straight, radially oriented cracks in the propellents of widths 1.27 mm, 1.016 mm, 0.762 mm, 0.508 mm, 0.254 mm, and 0.127 mm, placed at the tips of the star cavity.

Generation of a basic projection data set for the 0.9 deg angular increments was based on the Compton interaction alone for a photon energy of 310 keV. at 310 keV, very little photoabsorption takes place in the material in the phantom, including less than 7 percent of attenuation in the thin steel wall and a contribution to total attenuation on diameter of less than 0.5 percent. It should be pointed out that all of the simulated tomograms presented in this report are based on 100 percent detector efficiency for all energies.

It was then possible to utilize the basic set to calculate attenuation for the component lines in a polychromatic spectrum, by computing the energy dependent factor in the Compton cross-section for each and taking the ratio with that for the 310 keV value. In this way, attenuation data sets were obtained for the isotopic sources ^{192}Ir and ^{60}Co , using the weighted component strengths indicated in Table 1. These initial sets of data were free of statistical noise and of any scattering or detector miscalibration effects.

Reconstruction with the SMS filtered-back projection produced the two full frame tomograms presented in Figs. 8a and 8b for ^{192}Ir and ^{60}Co , respectively. The reconstruction grids were 64 pixels by 64 pixels in dimensions, with a pixel size of 3.6 mm x 3.6 mm. The two tomograms, each of which has been normalized to 1.5 g/cc in the region of propellant near the cork liner, are essentially identical. Based on two high-energy, source photons lying very close in energy, the ^{60}Co tomogram should be nearly equivalent to that for a monochromatic source. The ^{192}Ir beam undergoes a change in average peak energy from 367 keV to 410 keV along the on-diameter ray path of highest opacity.

Tomograms of the local region about each of the six cracks at the star tips are shown in Figs. 9 and 10 for ^{60}Co . In addition to the cracks, the oblique artifacts arising from the discrete point-to-point sampling are visible. Additional sampling, such as 800 views instead of 400, and spatial averaging due to finite geometry would lessen the relative importance of the artifacts.

An equivalent set of tomograms was generated for a 2.0 MeV bremsstrahlung source, with an average energy of 667 keV. As for the isotopic sources, the data was derived by a fit to the relationship between opacity values for the bremsstrahlung and the 310 keV line. A table of values was produced using a 200 point grid over the 2.0 MeV of photon energy, with each point weighted according to Equation (19). It was then fit with a second-order polynomial, providing coefficients for rapid and accurate conversion of opacity values for one source to those of another.

The results for the bremsstrahlung source were nearly indistinguishable from those for the isotopic sources above. It is advantageous at this point to introduce the use of a pattern recognition analysis to compare



FIGURE 8a. Simulated tomogram of 457 mm diameter rocket motor produced for an ^{192}Ir source. The symmetric pattern evident in the propellant region is interference due to the reconstruction grid.

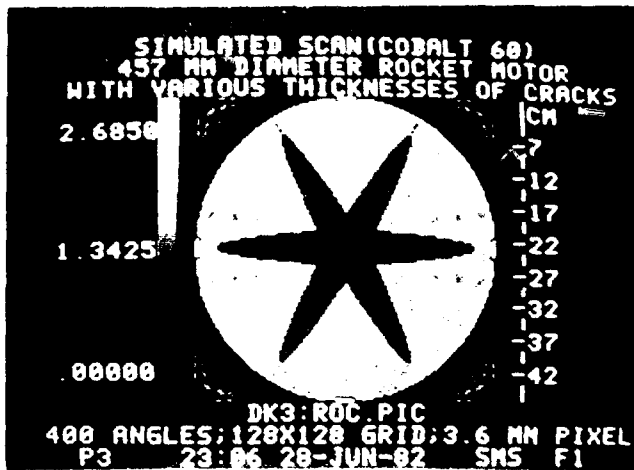


FIGURE 8b. Simulated tomogram of 457 mm diameter rocket motor produced for a ^{60}Co source.

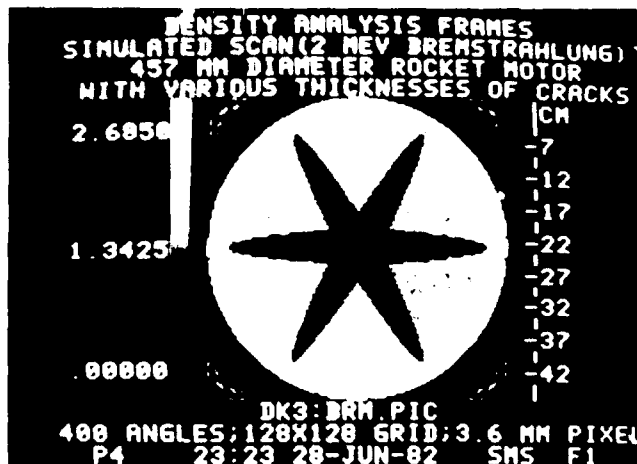


FIGURE 8c. Simulated tomogram of 457 mm diameter rocket motor produced for 2.0 MeV bremsstrahlung source. Density analysis frames are displayed on the vertical axis through the tomogram.

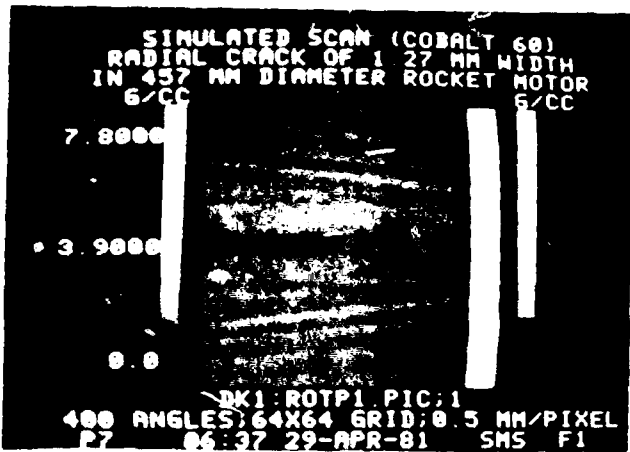


FIGURE 9a.

Region of simulated ^{60}Co
 tomogram including 1.27
 mm wide radial crack.

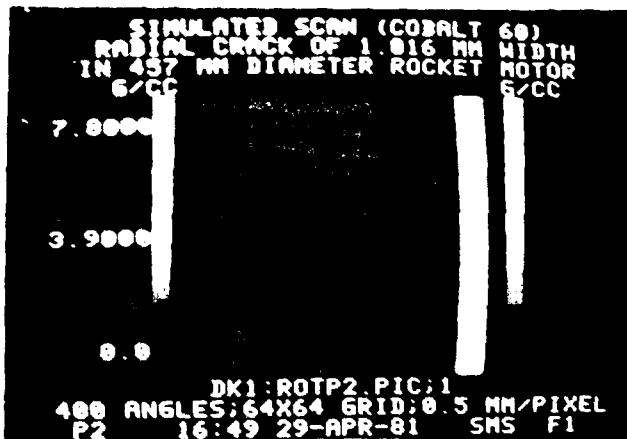


FIGURE 9b.

Region of simulated ^{60}Co
 tomogram including 0.016
 mm wide radial crack.

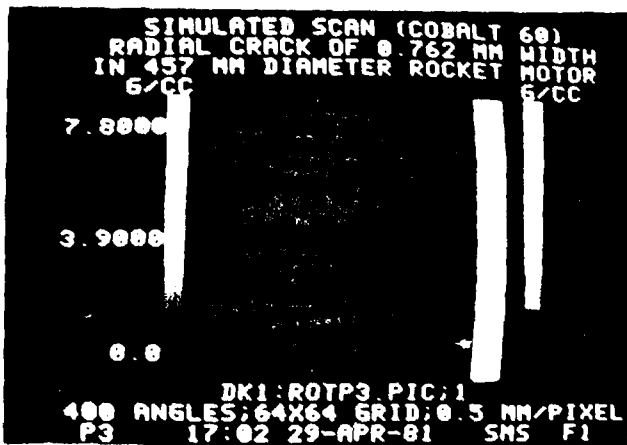


FIGURE 9c.

Region of simulated ^{60}Co
 tomogram including 0.762
 mm wide radial crack.

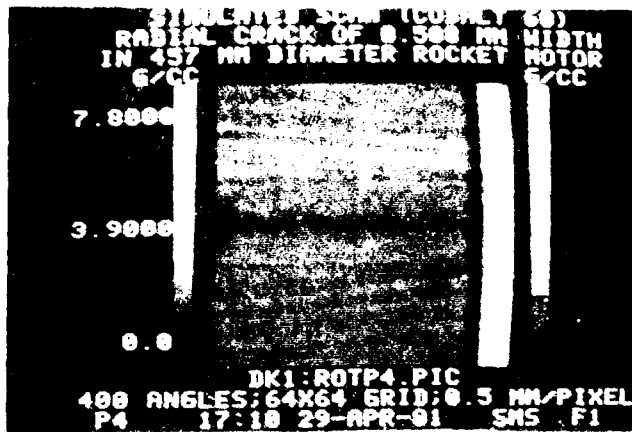


FIGURE 10a.

Region of simulated ^{60}Co
 tomogram including 0.508
 mm wide radial crack.

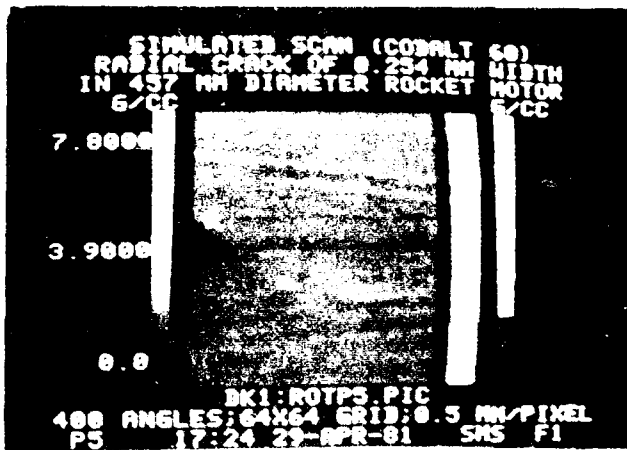


FIGURE 10b.

Region of simulated ^{60}Co
 tomogram including 0.254
 mm wide radial crack.

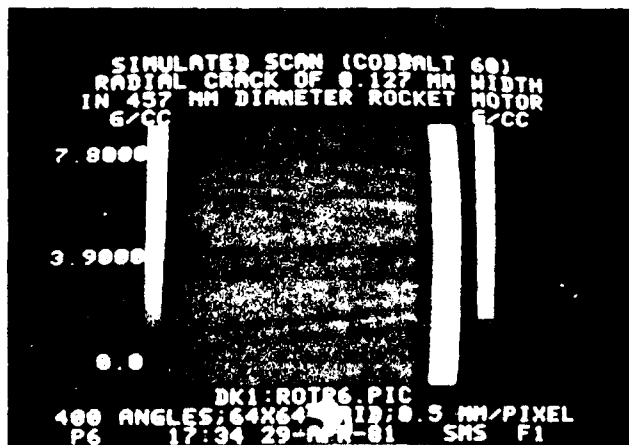


FIGURE 10c.

Region of simulated ^{60}Co
 tomogram including 0.127
 mm wide radial crack.

these and the other tomograms referred to in the following text. A more quantitative assessment of densities is needed than is provided by visual inspection of a black and white photograph. A numerical tabulation of the density values and variances serves that purpose. Such a tabulation is readily afforded by the digital form of the data, inasmuch as a tomogram is a two-dimensional matrix of density values.

The full frame tomogram produced by the 2.0 MeV bremsstrahlung source is shown in Fig. 8a, including demarcations of several local 18 mm x 18 mm regions along a radius, for which average density and variances have been obtained (see Table 8). The average density of the innermost region is only 9 percent below that of the outermost, indicating that the cupping or low density effect in the interior of a cylinder due to beam hardening is negligible in this case. In addition, the values are comparable to those for the ^{192}Ir and ^{60}Co cases, which are included in Table 8.

The variance is defined here in the usual fashion by the equation

$$\sigma^2 = \frac{\sum_{i=1}^n (X_i - \bar{X})^2}{n} \quad (23)$$

where the quantity X_i is the density value of the i^{th} pixel and n is the number of pixels within the region. While ordinarily a statistical quantity, the variance is used here as a measure of departure from an average value within a region due to other effects, such as artifacts and actual density variation. As will be shown below, it can serve as a sensitive indicator of the presence of cracks within a region of otherwise homogeneous density.

The frame analysis described above has been applied to the regions containing the radial cracks in all of the simulated tomograms. The frame size and location was the 5.5 mm x 5.5 mm frame displayed in Figure 11. The locations away from the crack are termed adjacent, and the one centered

TABLE 8. Average Densities^a Within Simulated Tomograms of 457 mm Phantom

Radius from Center (mm)	^{192}Ir	^{60}Co	2.0 meV Bremstrahlung
208.8	1.50	1.50	1.50
190.8	1.49	1.50	1.44
172.8	1.48	1.50	1.41
154.8	1.48	1.50	1.39
136.8	1.47	1.50	1.38
118.8	1.50	1.53	1.40
104.4	1.46	1.49	1.37
82.8	1.46	1.49	1.38

^a Densities in each case were normalized to 1.50 g/cc at a radius of 208 mm for comparison purposes.

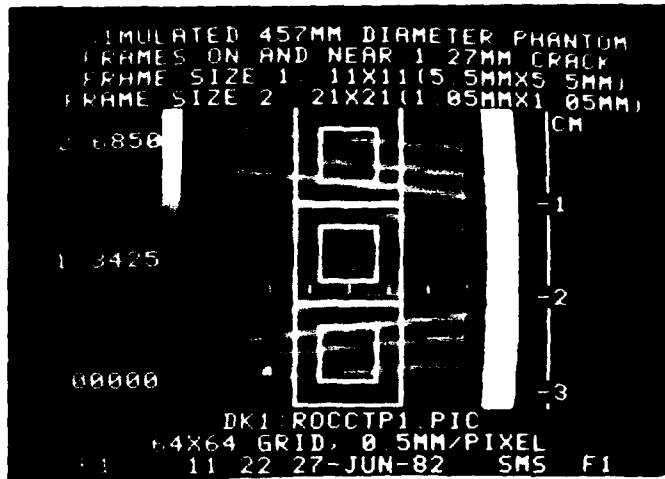


FIGURE 11. Region of 1.27 mm crack with two different sizes of analysis frames located adjacent to and on the crack: 11 pixels by 11 pixels (5.5 mm x 5.5 mm) and 21 pixels by 21 pixels (1.05 mm x 1.05 mm).

on the crack is termed on. Table 9 summarizes the density analysis for the crack regions. In actual practice, comparisons could be made between several different areas or between those expected to have high probability of flaws, such as the tip region, and those in between, expected to be relatively free of cracks. The intent here is to point out the usefulness of such a comparison.

As can be seen in the table, the presence of a crack within an area results in both a moderate decrease in average density and a substantial increase in variance, which acts effectively as a magnification of average density contrast. The size of the demarcation frame is not overly critical, within limits.

To provide an indication for at least one case of the effects of finite source and detector aperture on the visibility of the radial cracks, the data for the ^{60}Co case has been altered to include effectively spatial averaging. Each projection value in a view was averaged with the preceding and following ones. With a ray spacing at the detector assembly of 2 mm, that procedure approximated data for an array of detector elements 4 mm in width. The results are shown in Fig. 12c. Although boundaries are, of course, less distinct in the pictures, the frame analysis reveals anomalies almost as dramatic as those in the point-to-point case. The conservation of mass, or lack of it in this instance, provides a basis for detection even where the scale of spatial resolution is considerably larger than certain dimensions of the features of interest.

Further modification of the data set for the ^{60}Co simulation facilitated the introduction of inter-detector scattering effects directly into the opacity values. Based on the set of coefficients for case IA in Table 7, the original transmission values were used to fold together contributions

TABLE 9. Frame Analysis Values for Radial Cracks
in Computer Simulated Phantom

Source Crack Width (mm)	2.0 MeV Breinstrahlung		60 Co I ^a		60 Co II ^b		60 Co III ^c		60 Co IV ^d		60 Co V ^e	
	F (g/cc)	T ²	F (g/cc)	T ²	F (g/cc)	T ²	F (g/cc)	T ²	F (g/cc)	T ²	F (g/cc)	T ²
1.27 On	1.15	23.2	1.13	23.1	1.14	7.5	1.15	7.3	1.15	8.6	1.18	8.2
Adj.	1.50	1.03	1.49	1.46	1.51	0.13	1.52	0.12	1.52	0.75	1.55	0.10
Adj.	1.52	1.33	1.52	1.91	1.51	0.12	1.52	0.13	1.53	0.94	1.55	0.14
1.016 On	1.22	18.2	1.21	18.2	1.21	5.1	1.22	4.9	1.27	4.5	1.25	5.2
Adj.	1.49	0.72	1.48	1.01	1.51	0.13	1.51	0.12	1.53	1.12	1.54	0.13
Adj.	1.49	0.44	1.48	0.63	1.50	0.01	1.51	0.11	1.52	0.94	1.54	0.13
0.762 On	1.28	11.7	1.28	11.6	1.29	3.2	1.30	3.0	1.29	2.9	1.33	3.5
Adj.	1.50	0.50	1.49	0.71	1.50	0.10	1.50	0.10	1.50	0.93	1.54	0.09
Adj.	1.49	0.75	1.48	1.04	1.50	0.10	1.51	0.11	1.50	0.79	1.54	0.12
0.508 On	1.34	4.91	1.34	4.86	1.35	1.30	1.36	1.3	1.36	2.2	1.39	1.5
Adj.	1.49	0.88	1.49	1.26	1.51	0.14	1.52	0.13	1.51	0.79	1.55	0.13
Adj.	1.51	1.26	1.51	1.80	1.50	0.13	1.52	0.14	1.52	0.98	1.55	0.15
0.254 On	1.42	1.79	1.49	2.31	1.43	0.41	1.44	0.40	1.45	1.37	1.47	0.40
Adj.	1.49	1.25	1.49	0.60	1.51	0.13	1.51	0.12	1.52	0.97	1.55	0.13
Adj.	1.49	0.47	1.44	1.22	1.50	0.14	1.50	0.18	1.51	0.89	1.54	0.21
0.127 On	1.45	0.52	1.47	0.52	1.47	0.10	1.48	0.10	1.47	0.64	1.52	0.14
Adj.	1.50	0.49	1.50	0.70	1.50	0.17	1.50	0.16	1.50	1.02	1.54	0.17
Adj.	1.49	1.00	1.48	1.31	1.50	0.13	1.51	0.12	1.51	0.81	1.55	0.12

^a Point-source to point detector set

^b Spatially averaged set

^c Spatially averaged, uniform interdetector scattering

^d Spatially averaged, uniform interdetector scattering, random bias

^e Spatially averaged, corrected

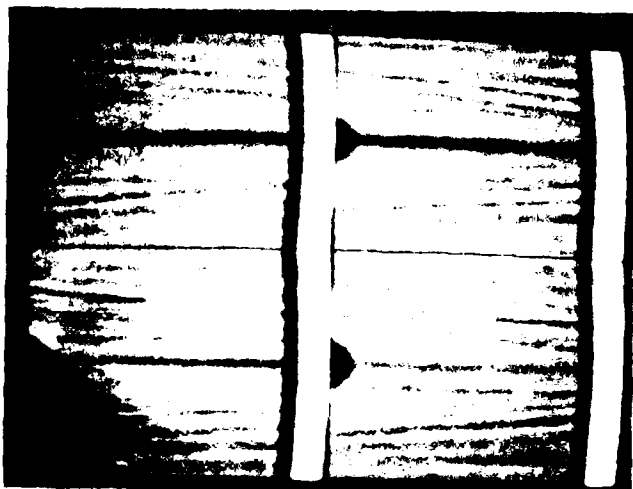


FIGURE 12a.

Simulated ^{60}Co tomograms of regions within 457 mm phantom containing radial cracks of widths: upper left - 0.762 mm; upper right - 0.508 mm; lower left - 0.254 mm; lower right - 0.127 mm.

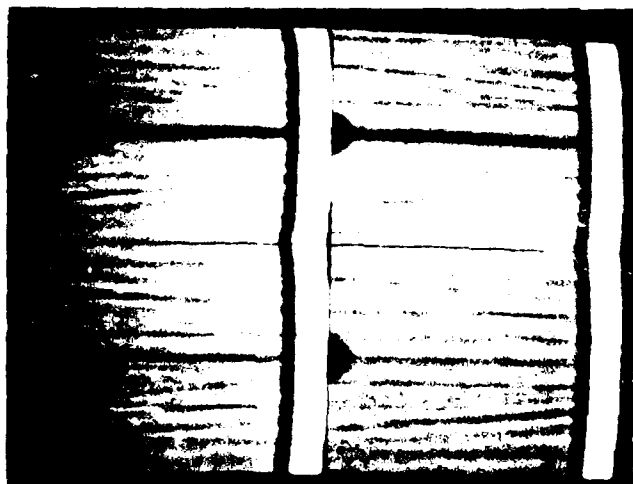


FIGURE 12b.

Simulated tomograms for the four smallest radial cracks produced using a 2.0 MeV bremsstrahlung source.

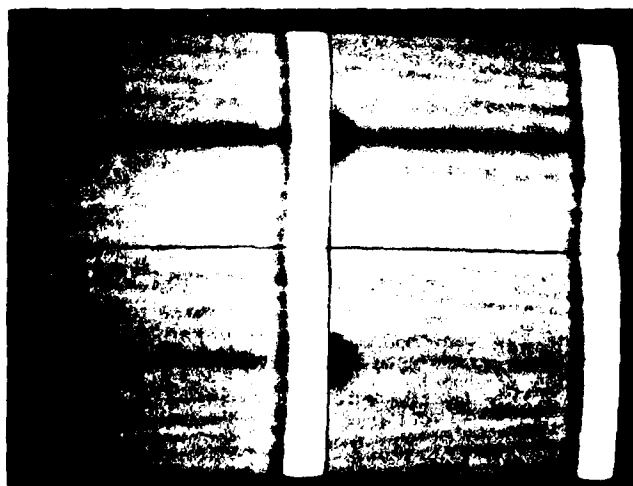


FIGURE 12c.

Same as Fig. 11a, except with spatially averaged rays rather than point-source to point-detector rays.

from neighboring detectors to produce a single total apparent transmission value for each ray path. The original tomogram of the largest radial crack in the phantom, and the corresponding one where inter-detector scattering has been incorporated via the Case IA coefficients, are shown in Fig. 13a. The inclusion of a perfectly uniform set of coefficients, which are identically the same for all detectors, only biases the density scale obtained for the tomogram but does not noticeably alter the features. It might be pointed out the gradual dependence of the object scattering pattern upon ray location, as indicated in the discussion above on object scattering, likewise would lead to little degradation in a high-contrast situation such as flaw detection within the solid propellant.

The critical source of error in the projection data is the unique response of a given detector to several factors. These include inter-detector scattering, severe object scattering, housing scattering, detector efficiency, and count-rate dependence and linearity over the dynamic range of interest. Housing scattering includes photons scattered into the detector assembly from any source other than object or another detector, such as floors, walls, and scanner shielding and structural support material. Scattering and detector miscalibration effects depend upon the particular physical and electronic configuration of the scanner system. A demonstration of the net effects of these factors has been accomplished by distributing biases randomly to the transmission values. Sets of data corresponding to detector subpositions were modified, where a given detector was assumed to be indexed to several different positions to accumulate data. Representing gross differences in characteristics of individual detectors, the major bias from subset to subset was chosen randomly, within a range of ± 0.5 percent the lowest transmission value in the entire projection set. A

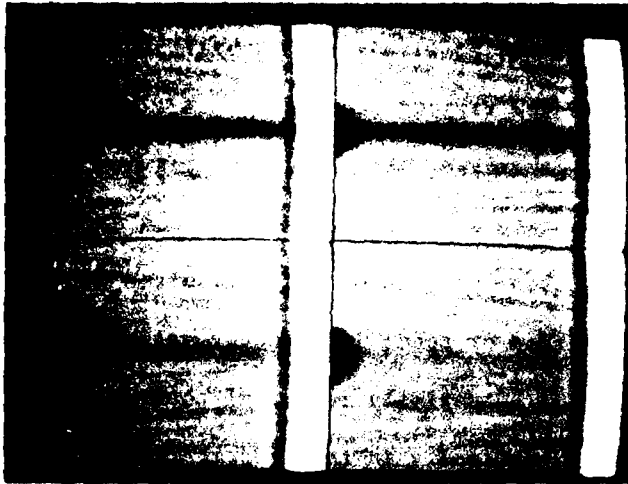


FIGURE 13a.

Spatially averaged ^{60}Co tomograms with addition of inter-detector scattering.

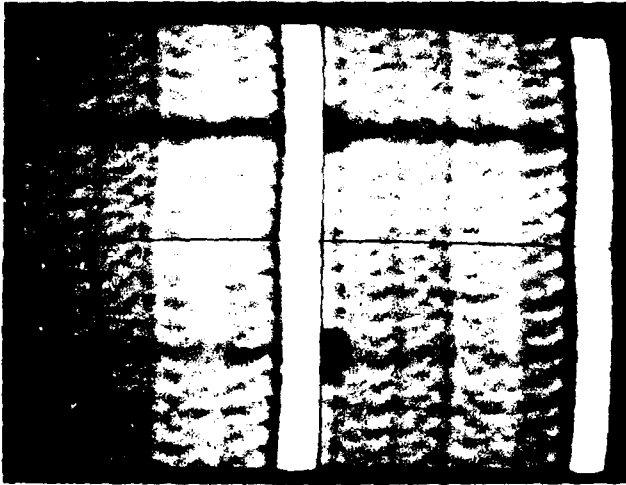


FIGURE 13b.

Results obtained when a random bias was added into the projection data which produced the tomograms in Fig. 13a. The bias simulated housing scatter and detector miscalibration.

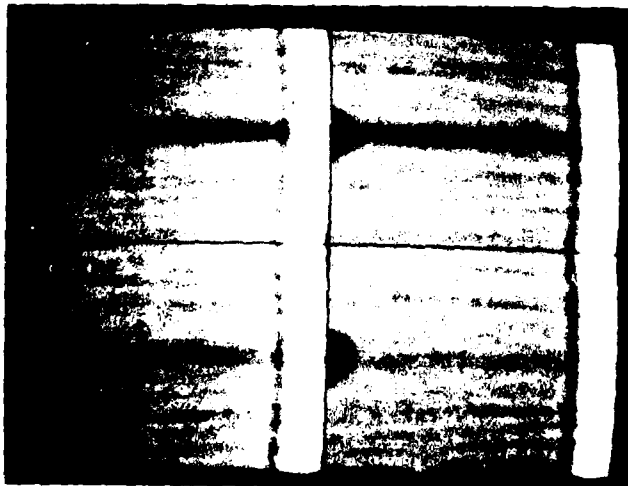


FIGURE 13c.

Results obtained when an SMS correction procedure was applied directly to the projection data producing Fig. 12b. Note the complete elimination of the ring artifacts.

secondary bias of ± 0.1 percent was distributed within each subset, to simulate nonsystematic fluctuations due to the various factors.

The substantial artifact pattern generated, including the ring or circular artifacts characteristic of rotate-only, TG geometries, can be seen in Fig. 13b. Use of an SMS correction procedure, which requires no prior knowledge of scattering coefficients or specific detector calibrations, yielded the result in Fig. 13c, which is essentially identical to Fig. 13a. The correction is based on an enforced continuity in the projection data. In addition to this simulation, it has proved effective in improving a large number of images of a variety of objects scanned with the SMS tomograph, including the rocket motor phantoms discussed below.

The frame analysis results in Table 9 for the simulations including scattering exhibit change only for the random bias case. The increase in the variance values is attributed to the increase in heterogeneity in density values arising from the presence of the artifacts. The removal of the ambiguity introduced by such fluctuations in detector response is obviously desirable for either visual or numerical interpretations of the tomograms.

2. NOSE REGION

Simulations have been completed of an approximation to the nose region of a rocket motor with the same 457 mm diameter mid-section. The source-to-detector distance of 122 cm used was the same as in the simulations of the mid-section. The nose geometry was simulated with a series of concentric, hemispherical shells. From outside to inside, they constituted the steel wall, cork layer, and solid propellant, respectively. The thicknesses of the shells were such that the radii to the boundaries in the tomographic plane were approximately 121 mm, 114 mm, 109 mm, and 50 mm, respectively. The tomographic slice plane was taken normal to the

longitudinal axis of the motor. The normal to the surface at the point of intersection with the plane made a 19° angle with respect to the plane (see Fig. 14).

The three-dimensional tomographic slice included a three-point longitudinal sampling at the detector, of equal spacing over a detector height of 5 mm. The vertical sampling was used to investigate the situation where the oblique surfaces near the nose region were scanned in such a geometry. The flaws, representing delaminations, consisted of crescent-shaped voids between cork layer and propellant, shown in Fig. 14 as the regions between the interior of the outermost hemisphere containing the propellant and the exterior of appropriately placed hemispheres of greater radii. The four voids, placed in quadrants in the object, were characterized by maximum vertical heights, in-plane widths and in-plane lengths (H, W, L) of (0.051 mm, 0.154 mm, 30.0 mm), (0.127 mm, 0.384 mm, 50 mm), (0.254 mm, 0.77 mm), and (0.508 mm, 1.55 mm, 98 mm), respectively.

The internal star-shaped cavity employed in describing the mid-section was omitted here, in order to minimize computer time for the simulation. It was felt the visibility of voids between layers would not be seriously degraded by the more complicated internal structure of the rocket motor. The data set was based on a scan of 400 angles and a 1 mm ray spacing (object center). The data was generated for a 2.0 MeV bremsstrahlung source with spatial averaging corresponding to a 4 mm detector width.

Tomograms for the regions of the largest and smallest voids are shown in Figs. 15a and 15b, respectively. Visually, it is very difficult to delineate areas with such low effective contrast from the surrounding medium. Accordingly, a region of the cork-propellant boundary with no flaws was brought into registration with the flawed regions and subtracted.

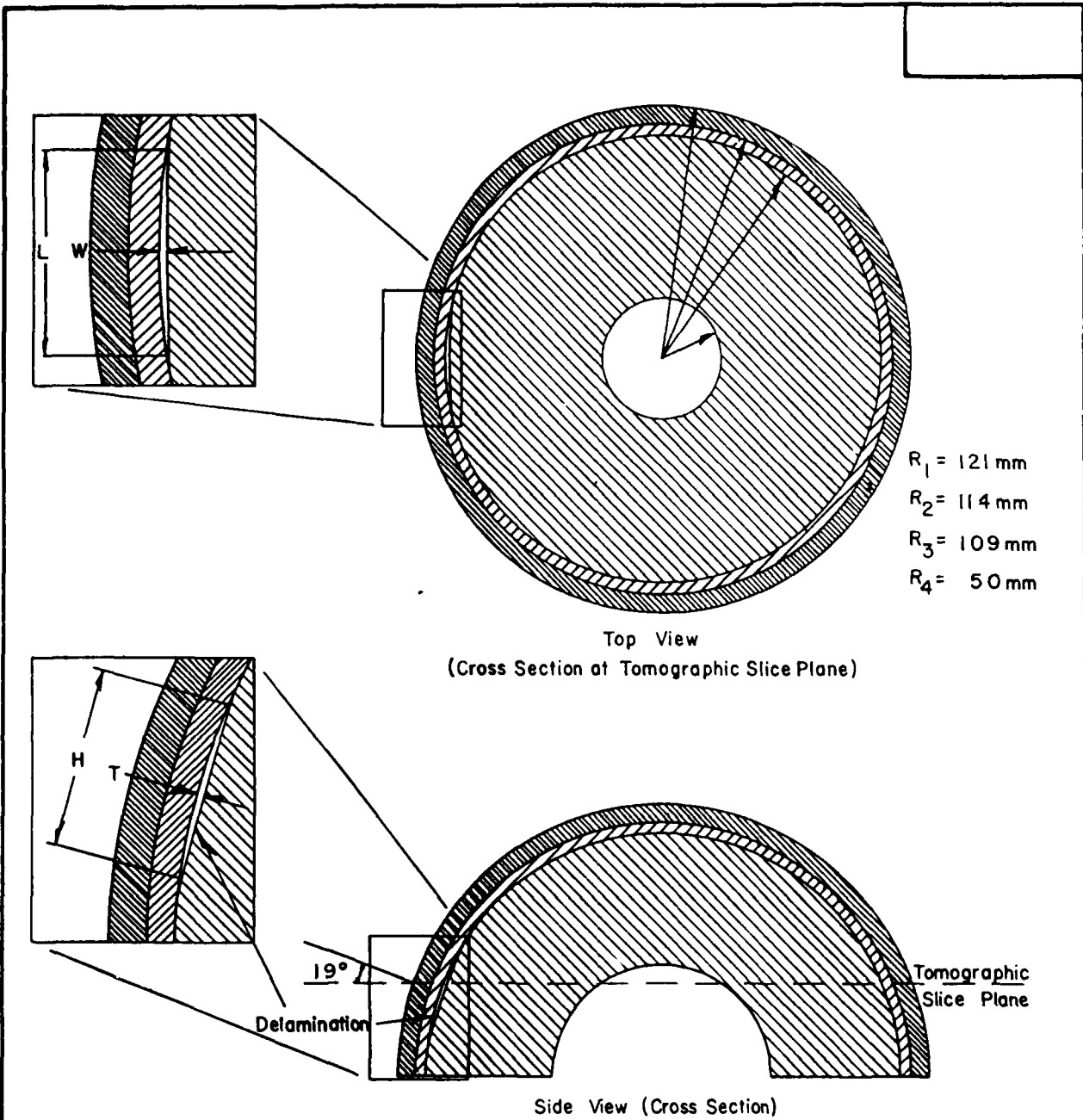


FIGURE 14. Drawing of geometry of simulated nose region.

SIMULATED NOSE REGION		
SCALE: 2/5	APPROVED BY	DRAWN BY
DATE: 5-25-62		T. R.
S.M.S. SCALE DRAWING		
		DRAWING NUMBER

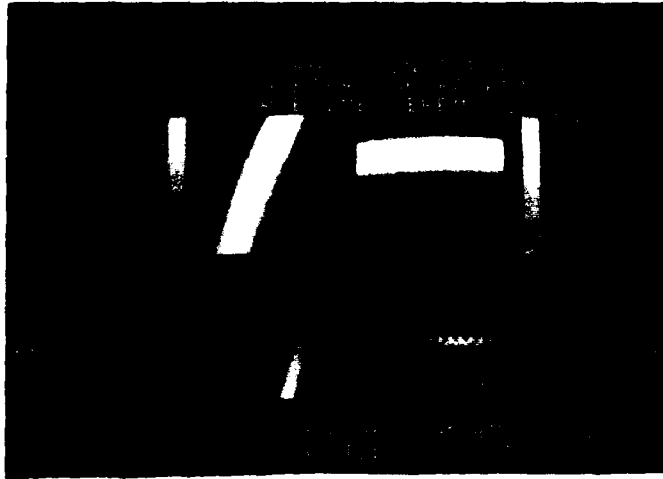


FIGURE 15a. (Upper left), tomogram of region of nose simulation containing largest delamination void (see text for details).

FIGURE 15b. (Upper right), region containing smallest void.

FIGURE 15c. (Lower left), tomogram of difference between Fig. 17a and an equivalent non-flawed region (scale maximum 3.0 g/cc).

FIGURE 15d. (Lower right), same result for Fig. 17b (scale maximum of 0.3 g/cc).

The resulting difference tomograms clearly reveal the flaw images, as can be seen in Figs. 15c and 15d for the largest and smallest flaws, respectively.

IV. EMPIRICAL SCANNING OF ROCKET MOTOR PHANTOMS

1. LARGE ROCKET MOTOR PHANTOM

a. Description of phantom - A rocket motor phantom was constructed of the approximate size and incorporating most of the features of the object simulated in the previous section. A scale drawing of the 47 cm diameter phantom is presented in Fig. 16 and a photograph in Fig. 17.

In order, from the outside to the inside, the phantom consisted of a 2.5 mm thick steel wall, and a 1.59 mm thick neoprene liner, a 1.59 mm thick cork layer ($\rho = 0.5$ g/cc), and a polyvinyl chloride (PVC) interior ($\rho = 1.42$ g/cc) to approximate the solid propellant. The neoprene was added to insure continuity of interfaces and to avoid gaps due to the lack of conformation of the steel about the PVC core.

In analogy to the simulation discussed above, radial cracks were placed in the PVC from the star tips to the cork, ranging in width from 1.2 mm down to 0.05 mm. All features in the phantom were constant over its 38 mm height in the longitudinal direction (normal to the tomographic slice plane). The dimensions of the internal cavity were very similar to that in the simulation, with star tips approximately 25 mm from the cork.

The widths of the three smallest radial cracks were determined by maintaining in place metallic gap strips of the appropriate thicknesses during the fabrication process and during scanning. The various machined PVC section of the phantom, as viewed in the cross sectional drawing, were glued to a circular PVC base. The base was slotted from center to perimeter radially through the area of the smallest crack. Metal straps were tightened around the steel shell, compressing the width of the small crack to the thickness of the tap strip.

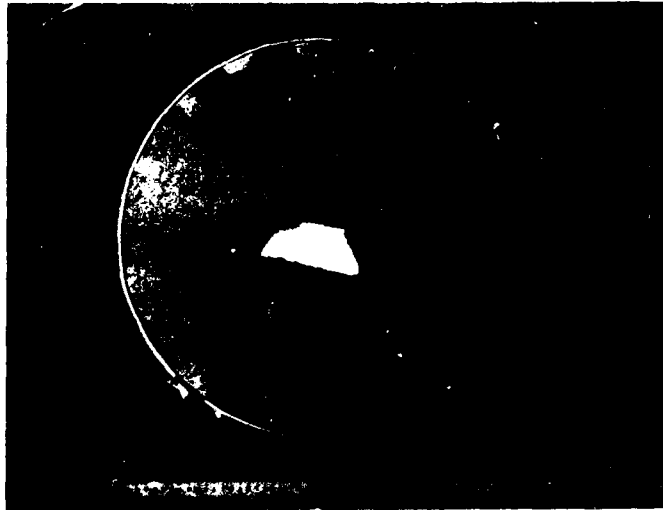


FIGURE 17a. Photograph of 470 mm diameter rocket motor phantom, prior to placement of holes and A rods in PVC. Note tape holding vertical steel calibration pin within the internal cavity.



FIGURE 17b. Tomogram of a 470 mm diameter phantom obtained from an empirical ^{60}Co scan. Breaks in the steel wall to the left and below center are due to intersection of the picture with the tomogram frame boundary. The break at lower left of center is a real space in the metal to allow for tightening of the steel ring.

The equivalent of delaminations were created by inserting rectangular plexiglass strips at two places on the perimeter between the cork and PVC. The strips were 7-9 mm in length along the circumference and in each case were spaced by over 3 mm. The two thicknesses used were 0.76 mm and 0.254 mm, which determined the spread between cork and PVC. Those thicknesses simulated delaminations of widths 0.76 mm and 0.254 mm.

Also, based on information from Mr. H. D. Cochran, the quality assurance manager at Hercules-McGregor in MrGregor, Texas, additional simulated flaws were placed in various regions of the mock propellant in the phantom, as indicated in Fig. 16. They included cylindrical holes with diameters of 5.6 mm, 4.0 mm, 2.8 mm, and 1.2 mm, representing voids, and cylindrical aluminum rods of diameters 1.6 mm and 0.8 mm, representing aluminum particles that inadvertently reside in a propellant having aluminum powder as a constituent. All of these features were aligned with longitudinal axis parallel to that of the phantom and constant over the 38 mm height.

b. Apparatus and Parametric Specifications -- The SMS EM-1 laboratory tomographic scanner used for the measurements has been in successful operation for over four years. It is configured in a fan beam geometry with a source to detector distance of 122 cm, as shown in Fig. 18. The detector system consists of 31 individual NE102 scintillation detectors coupled to phototubes, all housed in a light-tight aluminum box. Phototube output was processed in the pulse (photon) counting mode with amplifier/discriminators and recorded digitally in scalers. Cross-sectional dimensions of the detectors are 6.4 mm wide and 20.0 mm high, with lengths from 125 mm to 250 mm aligned radially from the source. The beam flux was collimated to a width of 2.4 mm and a height of 2.0 mm at each detector by lead detector apertures, with an interdetector spacing of ~ 8 mm.

TOMOGRAPHIC SCANNING SYSTEM

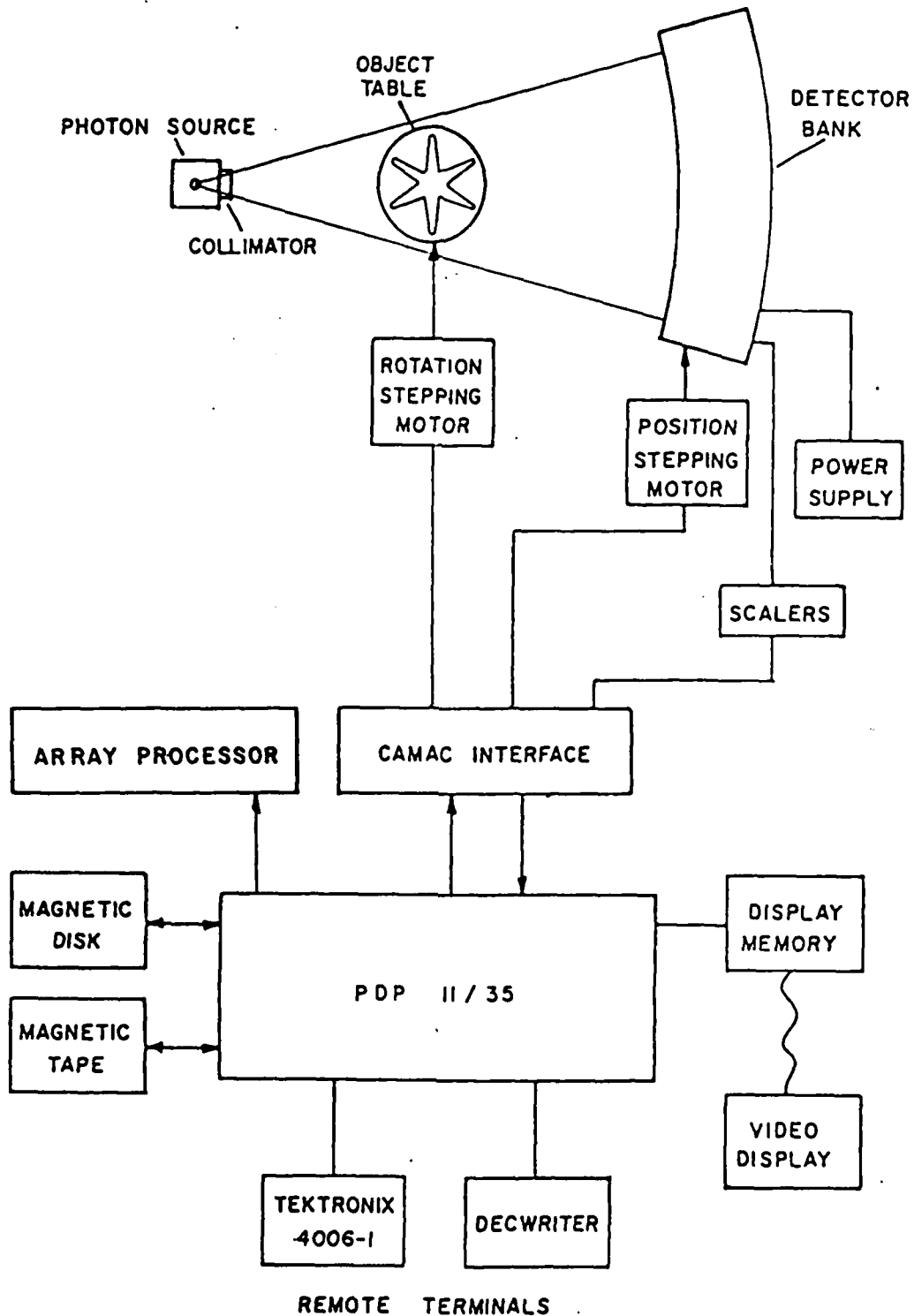


FIGURE 18. Block diagram of SMS industrial tomographic scanner system.

The photon source used in the scanning was a 50 Ci ^{60}Co source housed in a standard radiographic device (Gamma Industries Gammatron 50A). The housing includes sufficient depleted uranium shielding to reduce radiation rates to within acceptable values, according to applicable NRC and State Regulations. Additional shielding was provided to reduce radiation to negligible levels when the source was closed. The source was cylindrically shaped, with a diameter of 3.6 mm and a height of 2.0 mm. It was aligned with longitudinal axis coincident with the source-detector bank axis. With that orientation, the widest effective source width presented to a detector (either the first detector situation at -30 deg from the source-detector bank axis or the thirty-first detector at +30 deg) was only 4 mm. The air count rates (count rate with no object present) in the detectors in this configuration were ~ 400 kilohertz. The background counts, with appropriate phototube voltages and discriminator thresholds, averaged a few hundred herz. Source collimation restricted the primary flux to a solid angle which fell within that defined by the highly absorptive front face of the lead detector collimator assembly; in this method scattering was minimized. The height of the fan at the object was ~ 5 mm, with the dimension of the usable part of the flux being 2.0 mm, as determined by the source-detector sperture geometry.

The object table was positioned halfway between source and detector bank. The current SMS scanner operates as a modified "third generation" rotate-only tomograph. Given a fixed orientation of source and detector bank, the object table was rotated through 360 deg. Data accumulation occurred at regularly spaced angles within that range. The detector bank was then stepped sequentially to other positions within the angle defined by the axes of consecutive detectors, and the object rotation procedure

was repeated at each detector bank position. This procedure increased the density of ray paths defined within the fan. The resolution attainable with this configuration of the scanner has been determined to be ~ 1.2 mm at the center of rotation, as measured with a custom made resolution phantom.

As indicated in Fig. 18, the entire data taking process, with the exception of vertical positioning of the object (see below), was accomplished automatically, under control by a data acquisition program residing in the PDP 11/35. Positioning of the detector box, rotation of the object table, and periodic interrogation of the scalers recording the detection signals were performed in the above manner. Calibrations, including alignment of the detector bank to insure proper geometry and recording detector counts with no object in place ("air counts") for normalizing transmission counts, were completed prior to data accumulation.

Transmission data were accumulated for eight regularly spaced subpositions of the detector assembly over the inter-detector spacing of 1.38 cm, producing an angular spacing of 0.081 deg between adjacent ray paths. A total of 512 data points per view were obtained by recording data with the assembly in three major positions, which defined a fan angle encompassing the phantom entirely, and within each of which the subpositioning was accomplished. With a linear ray spacing of 0.9 mm at the center of the object, a 640 deg angle scan was performed, with 1.0 s exposure time at each combination of detector assembly and rotation table positions. Projection data were taken with a maximum statistical uncertainty of 1.5 percent in the individual opacity values and with a typical uncertainty from 0.5 percent to 1.0 percent.

The SMS correction procedure discussed above was applied to the opacity data prior to reconstruction with the filtered back projection algorithm.

Individual frames were reconstructed about each of the regions containing the simulated flaws.

C. Tomograms and Analysis -- The tomogram of the entire 470 mm phantom is presented in Fig. 17b. The projection data were corrected with the SMS correction procedure prior to reconstruction. The picture in 176 represents a scan of the phantom prior to the placement of the holes and aluminum rods in the PVC interior. Reconstructions of the areas around the six radial cracks are shown in Fig. 19.

The cracks are clearly visible down to 0.41 mm in width. The 0.15 mm crack is not discernible. An anomalous low density area appears in the region of the smallest crack, which appears to be due to a series of artifacts. The features of the anomaly include several striations which are spaced about at the sampling spacing and presumably involved a fluctuation in detector recording. Based on the decreasing visibility of the larger cracks, it is reasonable to assume that detection of the 0.05 mm crack was not accomplished in this particular scan.

Some remnants of the circular artifacts typical of a TG rotational scanning mode are still visible after the corrections, particularly in the tomogram of the 0.88 mm crack. As with the simulated data above, the features were all brought into the same approximate angular registration at the time of reconstruction. As a result, they can be viewed and analyzed more easily.

The regions of the simulated delaminations did not clearly reveal spacings between cork and PVC. However, as can be seen in Fig. 20, the 0.76 mm plastic strips themselves, of density 1.0 g/cc, are apparently visible. Isodensity marking of the same tomogram, set to a reduced range of 0 - 2.0 g/cc, defines boundaries of the strips more clearly. The

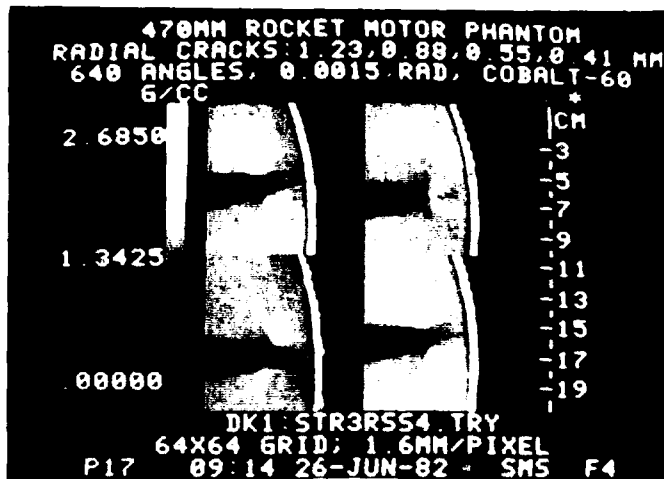


FIGURE 19a. Regions of empirical ^{60}Co tomogram of 470 mm phantom containing the following: upper left - 1.23 mm crack; upper right - 0.88 mm crack; lower left - 0.55 mm crack; and lower right - 0.41 mm crack.



FIGURE 19b. Regions corresponding to those above, containing: left - 0.15 mm crack and right - 0.05 mm crack.

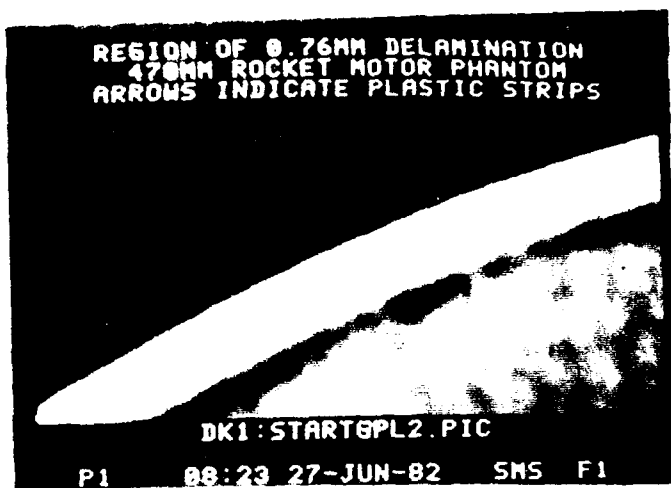


FIGURE 20a.

Tomogram of region of 470 mm phantom including two 0.76 mm thick plastic strips (see arrows) inserted between cork liner and PVC.



FIGURE 20b.

Tomogram of region in Fig. 22a, above, with density scale contracted and isodensity (black) markers at all pixels with densities in the range 1.1 - 1.2 g/cc. Note boundary definition of expected location of plastic inserts.

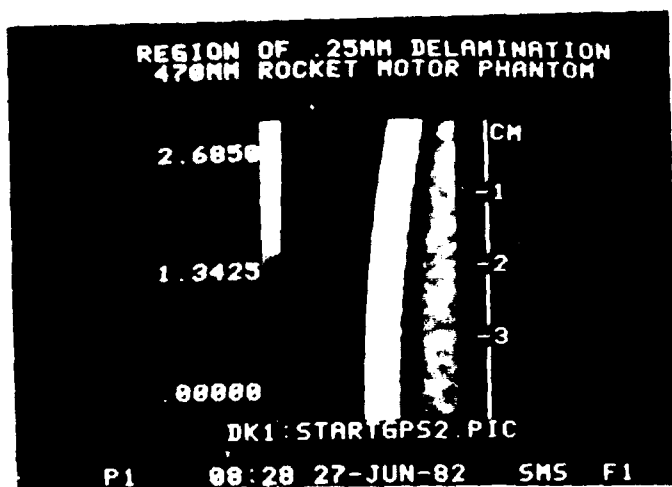


FIGURE 20c.

Tomogram of region of phantom including 0.25 mm thick inserts, with frame size twice that above.

feature of setting isodensity markers facilitates the interpretation of various regions of density with a single tomogram.

The low density region between the steel wall, which appears white in the figure, and the PVC which appears mid-gray, is in the 0.8 - 1.0 range. Those values are somewhat higher than the 0.5 g/cc of the neoprene and cork, presumably due to averaging with the higher density, neighboring materials. The 0.254 mm thick strips were not distinguished in the appropriate interface region.

Spatial resolution was judged to be ~ 3 mm for this scan, based on the degree of sharpness of various edges in the phantom. A scan with increased spatial resolution, on the order of $1 \sim 2$ mm, should reveal a feature with one dimension as small as 0.2 mm and a density contrast of 30 percent with its surrounding medium. The same applies to the 0.15 mm and even the 0.05 mm radial cracks, which are highly favorable targets for detection due to their straight edges.

The other simulated flaws included in the phantom for a second, identical scan with ^{60}Co are shown in Figs. 21 and 22. All of the cylindrical holes, representing voids in the propellant, are clearly visible in both locations. The 1.6 mm diameter aluminum rods are distinguishable but the 0.8 mm rods are not. There is a definite possibility the latter were not within the scan plane, as there was difficulty in inserting them into the PVC. The 1.6 mm rod represents a size of aluminum particle which could be detrimental to the performance of a rocket motor if it resided in certain locations.

Quantitative interpretation of the various features in the tomograms has been accomplished with the frame analysis applied above to the simulated phantom. The frame size and location for the radial cracks is indicated in Fig. 21. Similarly, frames centered directly on and adjacent to the

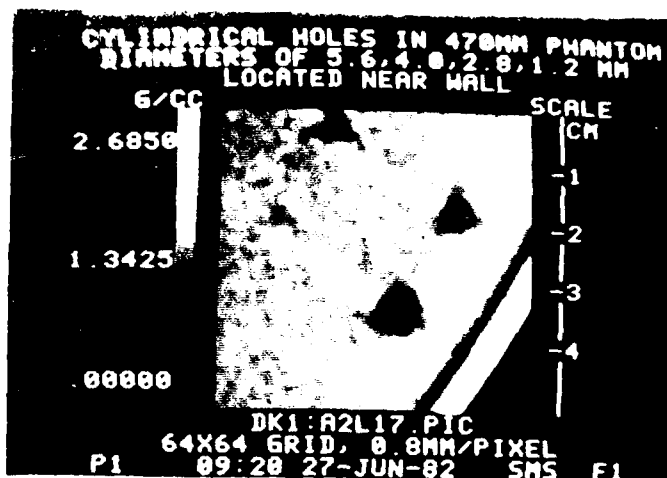


FIGURE 21a. Region of phantom near the steel wall containing group of four cylindrical holes with diameters (CCW starting from the bottom) 5.6 mm, 4.0 mm, 2.8 mm, and 1.2 mm.

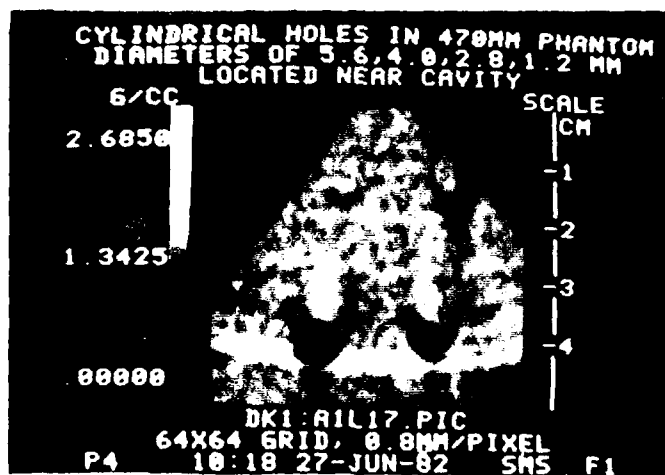


FIGURE 21b. Similar region as Fig. 21a near inside portion of internal cavity.



FIGURE 22a. Region of 470 mm phantom near the wall containing a 1.6 mm aluminum rod (above arrow).



FIGURE 22b. Region of 470 mm phantom near the center of the internal cavity containing a 1.6 mm aluminum rod (above arrow). Note circular artifact passing upper left to lower right, which causes apparent density comparable to that of the rod.

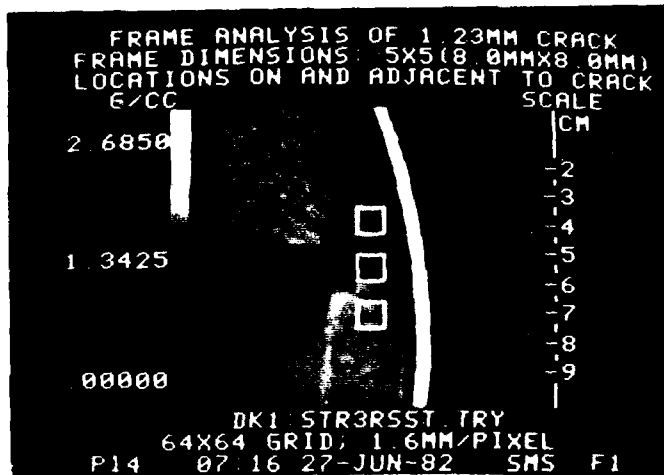


FIGURE 23. Tomogram of 1.23 mm crack in 470 mm phantom, with size (5 pixels x 5 pixels = 8.0 mm x 8.0 mm) and location of density analysis frame indicated (adjacent to and on the crack).

other features were used to extract average densities and variances. The extracted values are summarized in Tables 10 and 11.

As was the case with the simulations, the variance appears to be a sensitive indicator of the presence of cracks and the other high contrast flaws. A comparison of values can be obtained by sweeping a frame of appropriate size through critical areas of a tomogram. A computer search, complete with smoothing and enhancement routines, could reveal density variations difficult to discern visually.

An interesting possibility arises for characterizing the dimensions of flaws which are much smaller than the system spatial resolution. The effect of resolution is to distribute the mass or contrast of a relatively small feature over an area commensurate with the resolution. The total mass is conserved and is manifested in the change in average density over the region. If certain aspects of the geometry are known, or assumed, an estimate can be made of the true image size.

Using a nearly perfect example from the simulation data, values for Case I in Table 9 illustrate the technique. The average density within the frame on the 1.27 mm wide crack was 1.13 g/cc. The adjacent density was 1.50 g/cc. Three assumptions are: (1) the crack is singular; (2) it has 0 density; and (3) it proceeds from left to right across the frame. Then the mass deficit of 24.7 percent translates into a width of 24.7 percent of the frame width of 5 mm, or 1.24 mm. Similar agreement is found for the actual (extracted) widths of other cracks: 1.016 mm (0.91 mm), 0.762 mm (0.70 mm), and 0.508 mm (0.53 mm).

Such comparisons for cracks in the empirical tomograms are: 1.23 mm (1.74 mm), 0.88 mm (0.62 mm), 0.55 mm (1.32 mm), 0.41 mm (1.12 mm), and 0.15 mm (0). Given the quality of the empirical tomograms, an improvement

TABLE 10. Frame Analysis Values for Radial Cracks
in 470 mm Phantom

Crack Width (mm)	8.0 mm x 8.0 mm Frame	
	ρ (g/cc)	σ^2
1.23 On	1.08	6.4
Adj.	1.35	0.42
Adj.	1.49	0.50
0.88 On	1.30	2.8
Adj.	1.41	0.78
Adj.	1.41	0.43
0.55 On	1.11	2.6
Adj.	1.40	0.18
Adj.	1.26	0.47
0.41 On	1.28	1.37
Adj.	1.46	0.39
Adj.	1.52	0.46
0.15 On	1.62	0.90
Adj.	1.58	0.37
Adj.	1.58	0.52
0.05 On	1.12	1.84
Adj.	1.48	0.33
Adj.	1.27	0.42

TABLE 11. Frame Analysis for Aluminum Rods
and Holes in 470 mm Phantom

Diameter of Feature (mm)	5.6 mm x 5.6 mm Frame	
	ρ (g/cc)	σ^2
<u>Holes Near Wall</u>		
5.6	0.66	6.5
4.0	0.98	11.0
2.8	1.16	5.6
1.2	1.35	0.71
Adj.	1.46	0.38
<u>Holes Near Cavity</u>		
5.6	0.63	8.8
4.0	0.89	9.8
2.8	1.08	6.2
1.2	1.34	0.89
Adj.	1.39	0.31
<u>Al Rod Near Wall</u>		
1.6	1.55	1.39
Adj.	1.51	0.34
Adj.	1.46	0.20
<u>Al Rod Near Cavity</u>		
1.6	1.45	1.47
Adj.	1.37	0.22
Adj.	1.45	0.99

in picture quality could conceivably lead to reasonable accuracy in imaging of this type.

One extreme form of the frame analysis approach is a density trace one or a few pixels in width completely across a tomogram. Where a prior information is available about the object of interest, traces can be taken through critical regions and anomalies in them quickly noted. Density traces one pixel in width are displayed in Fig. 24 for the cracks in the 470 mm phantom. A proper fitting routine which searched for discontinuities in the differential of those traces would rapidly identify the presence of such flaws. The geometry of the path of search could be tailored to the characteristics of the object, as known or determined from the tomogram. For example, the region near the wall could be inspected by concentrating on a circular zone centered on the center of the rocket motor.

The empirical tomograms for the 470 mm phantom are essentially free of beam hardening effects. The use of a ^{60}Co source, which emits a nearly monochromatic spectrum, precludes any appreciable distortion due to hardening. However, as indicated in the computer simulated tomograms, tomograms produced with an appropriate bremsstrahlung source would likewise be essentially unaffected.

Substantial ring artifacts were removed from the tomograms by correcting for discontinuities in the projection data. The discontinuities are thought to have arisen largely due to interdetector scattering, which creates different responses in individual detector relative to transmitted signal strength. The correction procedure removed most all of the artifacts, with a few remnants visible. Certain of these are seen in the tomograms presented in this report. Substantial improvement would result, particularly in the quality of the uncorrected tomograms, if additional shielding and design changes were incorporated in the SMS detector assembly. Certain of these changes are now underway.

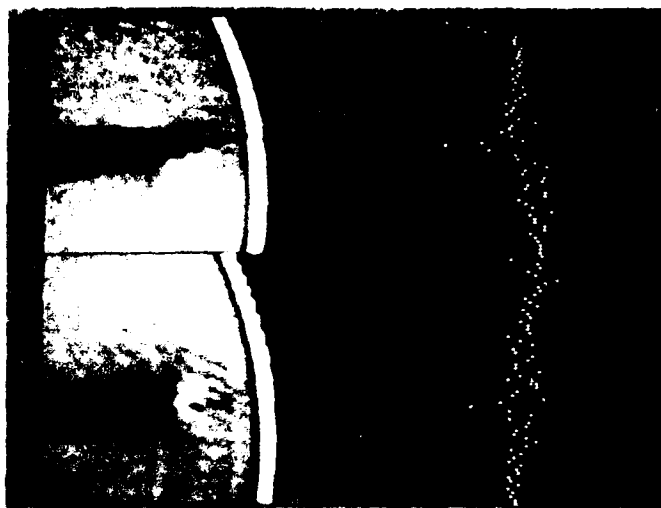


FIGURE 24.

Tomograms of radial cracks in Fig. 19, decreasing in width from the largest (top) to the smallest (bottom). To the right of each tomogram are the vertical traces 1 pixel wide at the position indicated by the arrows in the corresponding picture, with density scale in the horizontal direction. Note dip at location of a crack and anomalously large feature for smallest crack.



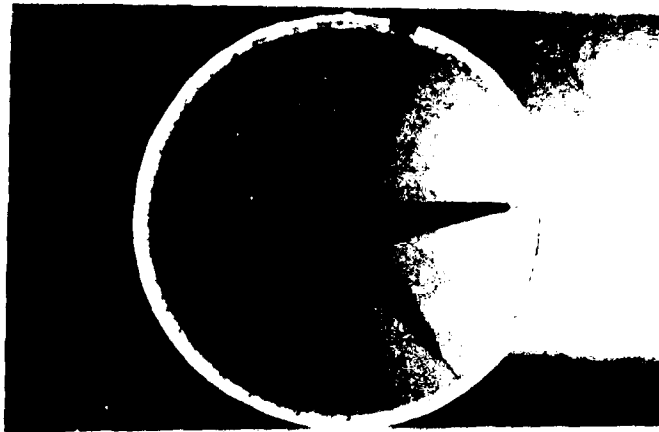
Even with the present system, the effects of scattering do not limit capability for flaw detection in the 470 mm phantom. The spatial resolution, on the order of 3 mm, would appear to be the primary factor limiting visibility of the smaller features. The simulated data implied that, with resolution of 2 - 3 mm, a 0.127 mm wide straight radial crack would be difficult to detect. Indeed, the 0.15 mm crack escaped detection. Other limitations should be mentioned at this point. The angular and ray sampling could both be increased substantially, resulting in some improvement.

2. SMALL ROCKET MOTOR PHANTOM

a. Fabrication and scanning -- A smaller version of the 470 mm diameter phantom was constructed utilizing an actual casing from a burned-out solid propellant motor, obtained from the project monitor at Wright Patterson Air Force Base. The casing was composed of a titanium alloy of wall thickness 3 mm and outer diameter 129 mm. A 1.6 mm thick cork liner was inserted around a machined PVC interior, with features scaled down essentially in proportion from those of the large phantom. No neoprene was used as in the large phantom. A photograph of the phantom is shown in Fig. 25.

Radial straight cracks of widths 1.0 mm, 0.75 mm, 0.5 mm, 0.15 mm, and 0.10 mm were placed, as for the larger phantom, from star tip to wall. Two 0.76 mm plastic strips were inserted between cork and PVC at one location.

The intent in the scanning of a second, smaller phantom was twofold. The first purpose was to investigate tomogram quality of a smaller object with similar flaws and the same source, where scattering should be less of a factor compared to the higher transmission rates. The second was to facilitate a higher degree of sampling in the region of the flaws, as is accomplished by using such an object scaled down by a factor of 3 and by increasing the ray density in the fan geometry. Accordingly, a 640 angle



83108 0.76

FIGURE 25a. Photograph of 129 mm diameter rocket motor phantom.

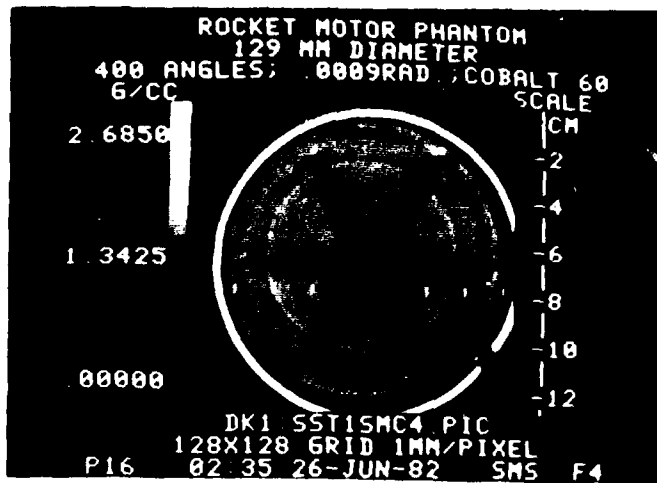


FIGURE 25b. Tomogram of essentially all of the 129 mm rocket motor phantom, produced with ^{60}Co . Breaks in wall at right and bottom are intersections with reconstruction boundary. Break in wall at lower right is a gap for tightening of the wall during fabrication of the phantom. Slight circular arcs visible in the PVC are artifacts.

scan with ^{60}Co was performed with a linear ray spacing at the center of the object of ~ 0.5 mm.

The regions of the radial cracks, in particular, were subject to a high density of sampling. Both large and small phantoms were centered on the center of rotation. For the former, the actual ray spacing in the fan at a given crack varied from 0.8 mm when it was oriented toward the source to 1.4 mm when it was closest to the detector assembly. The displacement of the crack due to the angular increment of the rotation table was 1.3 mm. With the increased sampling and smaller size of the second phantom, those quantities were reduced to 0.63 mm, 0.72 mm, and 0.5 mm, respectively.

b. Tomograms and Analysis -- The tomograms of the entire phantom and the individual features are displayed in Figs. 25b, 26, and 27. The 0.15 mm radial crack is clearly visible, in contrast to the result for the 0.18 mm crack in the larger phantom. Some circular artifacts remain after correction, but they do not appreciably detract from the visibility of the cracks. The 0.10 mm crack is not clearly seen, nor is it evident in the frame analysis results in Table 12.

The plastic strips were distinctly visible, as indicated in Fig. 27a. However, as with the larger phantom, the actual separation between cork and PVC was too slight to be clearly distinguished. In fact, definition of the cork itself was lacking, as seen in the density traces in Fig. 27b through the interface. The entire valley or dip in the traces between the plateau (PVC) and peak (steel) is only 3 mm in width. The cork at the boundaries is averaged in with the neighboring materials, exhibiting only at the bottom of the dip its actual density of 0.5 g/cc.

Density traces taken perpendicular to the cracks are included in Fig. 28. Based on the widths of the anomalies in the traces at the location of

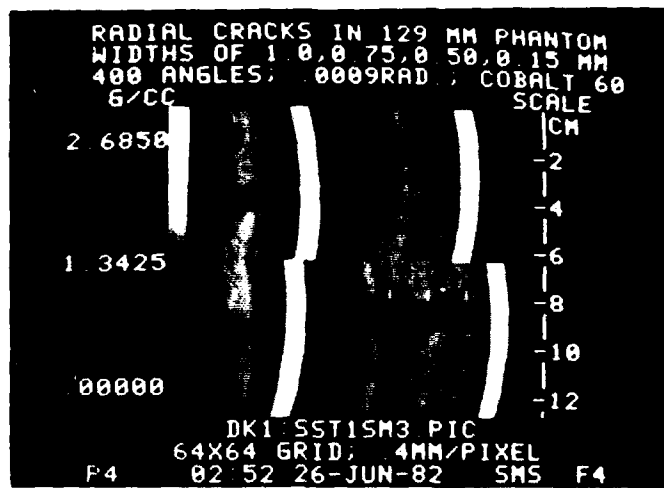


FIGURE 26a. Tomograms of regions in 129 mm phantom containing cracks of the following widths: upper left - 1.0 mm; upper right - 0.75 mm; lower left - 0.50 mm; and lower right -



FIGURE 26b. Tomograms at upper left and lower left include the 0.10 mm crack and no crack, respectively, in the same phantom. Opposite each tomogram to the right is a corresponding one with density scale altered so as to accentuate any possible density variations.



FIGURE 27a. Tomogram of region of cork-PVC interface containing 0.76 mm plastic inserts. Isodensity (white) markers are at all pixels with density values of 1.00 - 1.02 g/cc. Note boundary definition approaching the wall at the center of the picture, thought to be one of the strips.

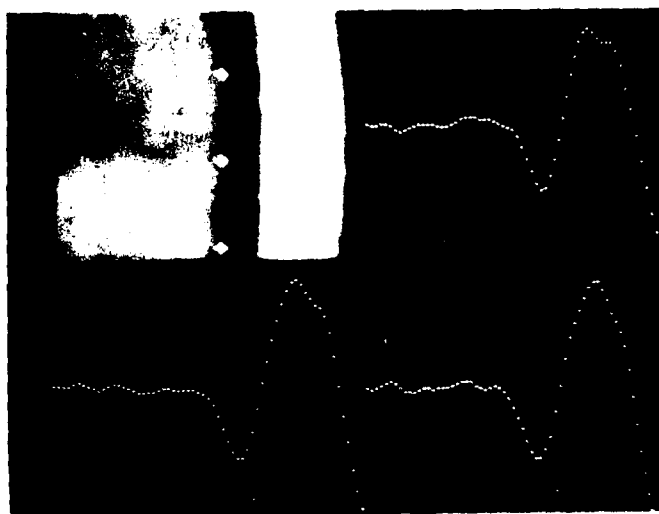


FIGURE 27b. Horizontal density traces 1 pixel (0.2 mm) high, taken at horizontal axes indicated by arrows in the tomogram of the PVC-cork-metal interface. The tomogram is based on a pixel grid of 64 x 64 and a pixel size of 0.2 mm x 0.2 mm. The traces are displayed with density scale from bottom to top in each quadrant.

TABLE 12. Frame Analysis Values for
Radial Cracks in 129 mm Phantom

Crack Width (mm)		2.8 mm x 2.8 mm Frame		4.4 mm x 4.4 mm Frame	
		$(\frac{P}{g_{lec}})$	σ^2	$(\frac{P}{g_{lec}})$	σ^2
1.0	On	1.01	1.52	1.11	3.34
	Adj.	1.33	0.15	1.32	0.26
	Adj.	1.35	0.12	1.37	0.26
0.75	On	1.22	1.42	1.26	1.28
	Adj.	1.34	0.12	1.34	0.14
	Adj.	1.36	0.11	1.37	0.09
0.50	On	1.21	1.20	1.26	1.57
	Adj.	1.40	0.43	1.41	1.01
	Adj.	1.39	0.67	1.37	1.54
0.15	On	1.27	0.32	1.31	0.77
	Adj.	1.41	0.16	1.41	0.11
	Adj.	1.42	0.06	1.43	0.08
0.10	On	1.42	0.11	1.44	0.24
	Adj.	1.41	0.05	1.41	0.09
	Adj.	1.45	0.11	1.45	0.21
0	On	1.54	0.18	1.51	0.51
	Adj.	1.50	0.08	1.51	0.12
	Adj.	1.36	0.43	1.37	0.80



FIGURE 28.

Tomograms from Fig. 31 displayed widest to narrowest crack, top to bottom. Opposite each tomogram is a vertical density trace 1 pixel (0.4 mm) wide, taken along axis indicated by the arrows. Density scale is from left to right. Note dips and location of cracks and lack of such a feature for the 0.1 mm crack and the crack-free regions at bottom.

the cracks, the spatial resolution in this scan was 1.8 mm. The definitions of the cracks in the traces and also in the frame analysis results in Table 12 are excellent. Other than the improvement in spatial resolution brought about by increased ray sampling, the quality of the tomograms is comparable to the results for the larger phantom. Scattering does not appear to be a major factor in either case.

V. CONCLUSIONS AND RECOMMENDATIONS

The simulations and empirical measurements described in this report indicate that beam hardening and scattering effects should not be serious obstacles in the use of computed tomography for non-destructive evaluation (NDE) of aerospace components. In the case of solid propellant rocket motors, in particular, the phenomena can be well documented both empirically and through the use of computer codes. Appropriate corrections may also be ascertained. Where objects of moderate total density and limited concentration of mass along straight paths are concerned, corrections for one or the other may even be unnecessary. Picture clarity may be sufficient initially to allow detection of high contrast flaws. If speed of image processing does not constitute a problem, appropriate corrections can be incorporated.

Beam hardening is especially straight forward to account for, regardless of the scanning geometry or the specific source and type of detector utilized. Isotopic sources, such as ^{192}Ir and ^{60}Co emission in the 300 keV - 1300 keV energy range, may require less of a correction. However, where composition of the object is essentially known or it is reasonable to assume that Compton scattering dominates the attenuation process, accurate mass corrections are readily available for bremsstrahlung sources as well. In the tomographic scanning of cylindrically symmetric objects with dispersed mass, such as rocket motors, hardening effects are minimal in any event.

Scattering is somewhat more difficult to characterize and depends largely on the amount of collimation and shielding incorporated in the scanning system. Interdetector scattering can be significantly reduced where insertion of proper shielding is possible. In the specific configurations investigated involving the ^{60}Co γ -rays of 1173 keV and 1330 keV energy, significant reductions were attained with as little as 0.4 - 1.6

cm of lead between detectors. Given the degree of shielding attainable, interdetector scattering coefficients can be measured and used through matrix methods to correct projection data. The approach used successfully in processing the empirical tomograms above to remove circular artifacts does not even require detailed measurements of individual detector. Considerations of the interdetector scattering processes do not indicate that any one of the three scanning configurations is clearly preferable. The fourth generation design may be slightly favored if a limited number of widely-spaced detectors are sufficient to produce the desirable image quality.

The relative importance of object scattering depends critically upon source energy, typical masses penetrated in the object, and collimation of source and detector. Simulations indicate that detector apertures of a few mm in dimensions may be needed to reduce the scattering to relatively low levels in the scanning of rocket motors. The second generation and third generation tomographic configurations, with fixed orientation of detectors relative to source, are definitely more appropriate where restrictive collimation is to be employed.

The fourth generation design requires that a detector accept source emission from anywhere within the shadow of the object. That condition precludes interception of photons scattered from anywhere within the tomographic plane through the object. The degree to which the scattering is detrimental can vary greatly, becoming insignificant only if transmission rates dominate scattering. The latter requirement may be difficult to satisfy for otherwise feasible combinations of source energy and mass of object. Another factor that should be considered is the need for detection of cracks and delaminations of tenths of a mm dimensions, within the rocket motors. If collimation is required to provide sufficient spatial resolution to

detect submillimeter flaws, the second or third generation approach may be the only feasible one.

The recommendations prompted by the research in this report are straightforward. Computed tomography appears to be a viable approach to NDE of rocket motors and its introduction in the general aerospace field should be pursued vigorously. Based on this preliminary work as well as other available reports of such studies, the second or third generation scanning configurations appear to be the leading candidates for rocket motor inspection.

The next step is to focus on performance specifications. Such specifications need to include motor size and mass, target flaw characteristics, speed of data acquisition and processing, and cost. Limits for those factors need to be defined for a particular case or group of cases, and detailed design studies should be initiated.

AD-A128 981 X-RAY COMPUTED TOMOGRAPHY FOR AEROSPACE COMPONENTS(U)
SCIENTIFIC MEASUREMENT SYSTEMS INC AUSTIN TX
F HOPKINS ET AL. JAN 83 AFWAL-TR-82-4128

22

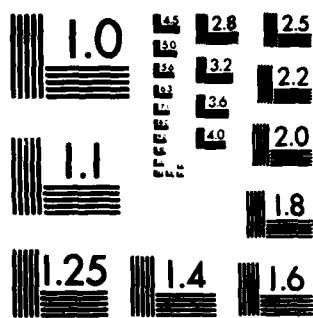
UNCLASSIFIED F33615-80-C-5145

F/G 20/6

NL



END
DATE
FILMED
7 83
DTIC



MICROCOPY RESOLUTION TEST CHART
NATIONAL BUREAU OF STANDARDS-1963-A

REFERENCES

1. Forrest F. Hopkins, Ira L. Morgan, Hunter D. Ellinger, Rudy V. Klinskiak, Glenn A. Meyer and J. Neils Thompson, "Industrial Tomography Applications," IEEE Transactions on Nuclear Science, Vol. NS-28, No. 2, April 1981; H. Ellinger, I. L. Morgan, R. Klinskiak, F. Hopkins, and J. Neils Thompson, "Tomographic analysis of structural materials," Proceedings of the Society of Photo-Optical Instrumentation Engineers, Vol. 182, Washington, D. C., April 19-20, 1979; I. L. Morgan, Hunter Ellinger, R. Klinskiak, and J. Neils Thompson, "Examination of Concrete by Computerized Tomography," American Concrete Institute Journal, Title No. 77-4, January-February 1980.
2. J. H. Hubbell, "Photon Cross Sections, Attenuation Coefficients, and Energy Absorption Coefficients from 10 keV to 100 GeV," U. S. Dept. of Comm., NSRDS-NBS 29, August, 1969.
3. NBS Circular No. 583.
4. C. M. Davison, "Interaction of Gamma Radiation with Matter," Chapter 1, Alpha-Beta-and Gamma-Ray Spectroscopy, K. Siegbahn (Ed.), Amsterdam, North Holland Publishing, 1965.
5. H. E. Johns and J. R. Cunningham, The Physics of Radiology, Charles C. Thomas, Springfield, Illinois, 1977.
6. P. M. Joseph and R. D. Spital, "A Method for Correcting Bone Induced Artifacts in Computed Tomography Scanners," J. Comp. Asst. Tomo. 2, pp. 100-108 (1978).
7. High Voltage Engineering Corporation Products Brochure, Burlington, Mass., June, 1979.

MED

8